Neutral Atom Lithography Using a Beam of Metastable Helium Collimated by Bichromatic Light

A Thesis Presented

by

Matthias Paul Riedmann

to

The Graduate School

in Partial Fulfillment of the Requirements

for the Degree of

Master of Arts

in

Physics

Stony Brook University

August 2005

Stony Brook University

The Graduate School

Matthias Paul Riedmann

We, the Thesis committee for the above candidate for the Master of Arts degree, hereby recommend acceptance of the Thesis.

Distinguished Teaching Professor Harold Metcalf, Thesis Advisor

Department of Physics and Astronomy, Stony Brook University

Professor Alexander Abanov, Chairman of Defense

Department of Physics and Astronomy, Stony Brook University

Professor Michael Rijssenbeek

Department of Physics and Astronomy, Stony Brook University

This Thesis is accepted by the Graduate School.

Dean of the Graduate School

Abstract of the Thesis

Neutral Atom Lithography Using a Beam of Metastable Helium Collimated by Bichromatic Light

by

Matthias Paul Riedmann

Master of Arts

in

Physics

Stony Brook University

2005

Forces of electromagnetic light fields on atoms have been studied for more than two decades. Most of the research effort has focused on monochromatic forces, but these are either limited by atomic parameters (radiative force) or their direction changes on the wavelength scale (dipole force). Today, after being thoroughly studied and despite their limitations, these forces are effectively used for slowing and collimating of atomic beams and for cooling of atomic ensembles (optical molasses). Introducing a second frequency to the light field enables coherent exchange of momentum between the field and atoms, which

results in a force of significantly larger magnitude. This bichromatic force is effective on macroscopic scales and does not saturate for high intensity. We use it for collimation of a metastable helium beam. In combination with an additional optical molasses collimation stage, the brightest metastable helium beam ever has been created in our lab [2].

The study of light-induced forces on atoms has resulted in subwavelength control of atomic motion which opened up the field of atomic nanofabrication [22]. In the work presented here, we combine bichromatic collimation of an atomic beam and neutral atom lithography for the first time. Unlike optical lithography, this method is not limited by diffraction because the de-Broglie wavelength of the atoms forming the beam is on the sub-atomic scale. Metastable helium is especially applicable for this purpose since it carries high internal energy that can damage a hydrophobic monolayer of organic (alkanethiol) resist molecules. Permanent structures are created by a wet-etching process which attacks the top layer (gold) of the lithography samples where the resist is damaged. Due to the high internal energy of metastable helium, a dose of only $2.8 \times 10^{12} \frac{He^{*}\ atoms}{mm^{2}}$ which corresponds to 0.59 atoms per resist molecule, is sufficient to get good contrast in the etching process. This dose requires an exposure time of 20 minutes. Scans with an atomic force microscope reveal the high resolution of 63 nm we achieve with this method.

To my family and friends

Contents

List of Figures ix

List of Tables xi

Acknowledgements xii

1 Theory and Experimental Basics 1

1.1 Monochromatic Forces 2

1.1.1 Radiative Force 2

1.1.2 Velocity Dependence 4

1.1.3 Optical Molasses 5

1.1.4 Cooling of Multi-Level Atoms 8

1.1.5 Dipole Force 8

1.2 Bichromatic Force 10

1.2.1 Rabi Oscillations 11

1.2.2 π-Pulse Model 12

1.2.3 Bichromatic Force Simulation 16
1.2.4 Bichromatic Collimation 17
1.3 Atomic Nanofabrication 20

2 Vacuum System 26
2.1 Metastable Helium Source 26
2.2 Beamline 31
2.3 Sample Loading Chamber 34
2.4 He* Detection 35
2.4.1 MCP/Phosphor Screen 36
2.4.2 Stainless Steel Detectors 38

3 Laser System 42
3.1 Light Production 42
3.2 Frequency Locking 48
3.3 Four Frequency Production 51
3.4 Amplification 52
3.5 Preparing the Beams for Bichromatic Collimation 54
3.5.1 Phase Matching 54
3.5.2 Frequency Balancing 55
3.5.3 Beam Expansion 56

3.5.4 Beam Recycling 57
3.5.5 Polarization and Optical Pumping 58
3.6 Optical Molasses Stage 60

4 Neutral Atom Lithography 63
4.1 Samples 63
4.2 Self-Assembled Monolayer (SAM) 65
4.3 Wet Etching 67

5 Results 71
5.1 He* Flux Measurement 71
5.1.1 MCP/Phosphor Screen 72
5.1.2 SSD Measurements 74
5.2 Lithography 80
5.2.1 Atomic Force Microscope (AFM) 80
5.2.2 Results 81
5.2.3 Resolution 87

6 Conclusion 92

Bibliography 94

A Atomic Beam Profile 99

List of Figures

1.1 Optical Molasses 6

1.2 Rabi Oscillation 12

1.3 Illustration of the π-Pulse Model 14

1.4 Bichromatic Force Profile 17

1.5 Force Profile for Bichromatic Collimation 18

1.6 Bichromatic Collimation Frequency Spectrum 19

1.7 Relevant Energy Levels of He 23

2.1 Metastable Helium Source 28

2.2 Vacuum System 32

2.3 Sample Holder 35

2.4 MCP/Phosphor Screen Detector 36

2.5 Stainless Steel Detector 40

3.1 Laser Setup 43

3.2 Laser Diode Power Output 46

3.3 Diode and Extended Cavity 47

3.4 Frequency Locking System 49

3.5 Four-Frequency AOM 51

3.6 Laser Beam Arrangement for Bichromatic Collimation 58

3.7 Sublevels of 2^3S_1 and 2^3P_2 59

4.1 Sample in Several Lithography Steps 68

5.1 Different Collimation Methods Viewed by MCP/PS 73

5.2 3D Surface Plot of Collimated Atomic Beam 76

5.3 Atomic Beam Cross Section 77

5.4 AFM Picture of Well Etched and Exposed Sample 82

5.5 AFM Picture of Underexposed Sample 84

5.6 Lineout of AFM Picture 86

5.7 Detail Scan for Analysis of Resolution 88

5.8 Lithography Resolution 89

A.1 Atomic Beam Cross Section, Big SSD Slit at 2.5 cm 99

A.2 Atomic Beam Cross Section, Big SSD Slit at 2.8 cm 100

A.3 Atomic Beam Cross Section, Big SSD Slit at 2.9 cm 100

A.4 Atomic Beam Cross Section, Big SSD Slit at 3.0 cm 101

A.5 Atomic Beam Cross Section, Big SSD Slit at 3.3 cm 101

List of Tables

1.1 Properties of Experimental Transition 22

3.1 Spot Sizes of the Bichromatic Beams 56

4.1 Wafer Specifications 64

4.2 Components of the Etching Solution 69

Acknowledgements

The work presented here would have been impossible without the help, support and advice of many people. First of all I have to thank my advisor Hal. He convinced me to join this group and increased my interest in atomic physics. He managed to transfer his enthusiasm for AMO physics to me and could always give me the right advice. It was a pleasure to work in his group.

I enjoyed working with Claire, Matt E., Matt P. and Xiyue on the bichromatic collimation/lithography experiment, even though the setup gave us trouble sometimes. They and the other people in the lab, Mr. Lee, Olkseii and Oleg told me all the skills that are necessary to run such an experiment.

The time here at Stony Brook would have been very sad without my friends, both here in the US and at Germany. Thanks for all the emails, the visits and the fun we had.

I owe my warmest thanks to my family who encouraged me. I could always rely on your advice and support.

I am indebted to everybody who is responsible for the exchange program between the physics departments of Würzburg and Stony Brook. I hope this cooperation will stay active and give many students the opportunity to study abroad.

This work was supported by the German Academic Exchange Service (DAAD) and the Research Foundation of State University of New York.

Chapter 1

Theory and Experimental Basics

The description of electromagnetic forces on atoms can use a quantized picture of the electromagnetic field. The field is build up by quanta called photons, which carry a certain amount of momentum $\mathbf{p}$ and energy E.

$$\mathbf{p} = \hbar k \qquad\qquad E = \hbar\omega = |\mathbf{p}|\, c \tag{1.1}$$

$k = \frac{2\pi}{\lambda}$ is the wave vector, ω the angular frequency and λ the wavelength. These are related by the speed of light c.

$$c = \frac{\lambda\omega}{2\pi} \tag{1.2}$$

The observable quantities, wavelength and frequency, indicate that this concept works well for monochromatic light fields. Therefore, forces from monochromatic light will be discussed first.

1.1 Monochromatic Forces

Monochromatic light forces have been studied for more than 20 years. If the light frequency is close to a non-degenerate, dipole-allowed atomic transition, the interaction between electromagnetic field and atom is dominated by this transition. In this case, the contribution of other levels is small and can be neglected, leading to the picture of the two-level atom. The two involved levels are called ground state and excited state.

The exchange of energy and momentum between atom and light field is described by absorption, stimulated emission and spontaneous emission [9]. Equation 1.1 describes the amount of energy and momentum, which is exchanged in these processes.

1.1.1 Radiative Force

An atom in an unidirectional light field is affected by the radiative force. The atom absorbs a photon and gets its momentum $\hbar\mathbf{k}$. If the subsequent emission is stimulated, the emitted photon carries $\hbar\mathbf{k}$ and the net momentum transfer vanishes. If no decay is induced, a photon is emitted spontaneously after an average, level-specific lifetime τ. The direction of this emission is random and can be described as an isotropic process in the average over many cycles. This leads to a net momentum exchange of $\hbar\mathbf{k}$ between atom and light field for each absorption–spontaneous emission cycle.

The second important factor to the resulting force is the rate of absorption that produces spontaneous emission γ_p (scattering rate):

$$\gamma_p = \frac{s_0\gamma/2}{1 + s_0 + (2\delta/\gamma)^2} \tag{1.3}$$

In this formula, several important quantities are introduced. $\gamma = \frac{1}{\tau}$ is the natural linewidth, $\delta = \omega - \omega_a$ is called detuning and describes the difference between laser frequency ω and atomic resonance ω_a. $s_0 = I/I_s$ is the saturation parameter with the saturation intensity I_s:

$$I_s = \frac{\pi hc}{3\lambda^3\tau} \tag{1.4}$$

With the momentum of (1.1), the radiative force $\mathbf{F}_{rad}$ is given by:

$$\mathbf{F}_{rad} = \hbar\mathbf{k}\gamma_p = \frac{\hbar\mathbf{k}s_0\gamma/2}{1 + s_0 + (2\delta/\gamma)^2} \tag{1.5}$$

For high intensity, stimulated emission dominates over spontaneous emission. This leads to saturation of the radiative force for high intensity ($s_0 \gg 1$ and $s_0 \gg \frac{2\delta}{\gamma}$). The maximum magnitude of the radiative force is defined by atomic parameters and independent of the light field.

$$\mathbf{F}_{rad,max} = \frac{\hbar \mathbf{k} \gamma}{2} \tag{1.6}$$

1.1.2 Velocity Dependence

The discussion above did not consider the movement of atoms. In this case, the external frequency gets shifted in the rest frame of the atom (*Doppler effect*). In a linear approximation for small velocities, the Doppler shift is proportional to the velocity component along the light beam.

$$\delta_{Doppler} = -\mathbf{k} \cdot \mathbf{v} \tag{1.7}$$

If this shift is positive, it is called *blue*, whereas a negative detuning is called *red*.

One of the standard applications for the radiative force is deceleration of atomic beams. This beams are often created by evaporation of atoms at high temperatures, leaving atoms with energies determined by this temperature. To slow down such an atomic beam, a counterpropagating, red detuned laser is used. The detuning compensates the Doppler shift and affects only atoms of a certain finite velocity. However, the radiative force is only effective over a relatively small velocity range. Effective slowing of atomic beams (laser cooling) therefore needs dynamic adjustment of the laser or the atomic resonance frequency. The latter is usually done in a magnetic field whose magnitude changes along the atomic beam [18]. This Zeeman slower method became standard for the loading of neutral atom traps, which are used widely in AMO research.

The velocity dependence through the Doppler shift indicates that the radiative force is not conservative. The reason lies in the nature of spontaneous emission, which dissipates energy out of the atom-light field system. This is a very important aspect of laser cooling since dissipative forces allow phase space compression of atom ensembles.

1.1.3 Optical Molasses

Two counterpropagating, slightly red detuned laser beams can be used to reduce the velocity of atoms in one dimension to very small values. This works analogous to the radiative force. The red detuning makes absorption more likely, if an atoms moves against the direction of $\mathbf{k}$. Since there is a laser beam incident from each side, atoms at $v = 0$ do not experience a net force, because absorption from either beam occurs with the same probability. The force caused by each beam is equal to the radiative force. To take finite atomic velocities into account, the effective detuning is given by the actual laser detuning δ and the Doppler shift.

$$\mathbf{F}_{\pm} = \pm \frac{\hbar \mathbf{k} \gamma}{2} \frac{s_0}{1 + s_0 + [2(\delta \mp \mathbf{k} \cdot \mathbf{v})/\gamma]^2} \tag{1.8}$$

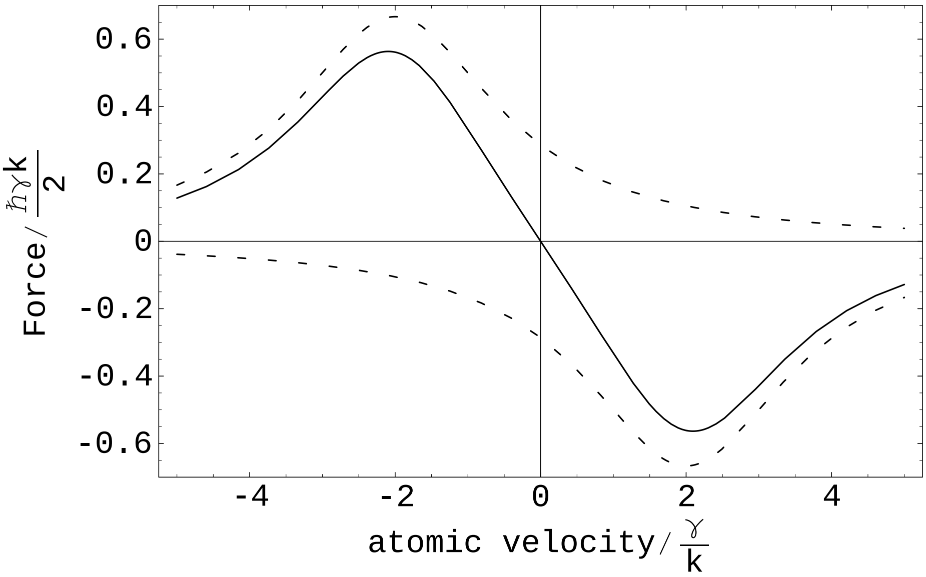

Figure 1.1 Force profile of optical molasses. The parameters for this plot are $\delta = \gamma$, $s = 2$. The dashed lines illustrate the contributions from $F_{\pm}$.

The sum of $\mathbf{F}_+$ and $\mathbf{F}_-$ is shown in figure 1.1. Atoms of low velocity experience a force which opposes their motion. This damping force can be derived from equation (1.8) for the case $\frac{\mathbf{kv}}{\gamma} < 1$ (nonlinear contributions are neglected).

$$\mathbf{F}_{OM} \simeq \frac{8\hbar k^2 \delta s_0 \mathbf{v}}{\gamma \left(1 + s_0 + (2\delta/\gamma)^2\right)^2} = -\beta \mathbf{v} \tag{1.9}$$

Note the factor of δ in the numerator of β. This indicates that only red detuning leads to an effective damping force. This principle can also be extended to two or even three dimensions with four/six laser beams. In the latter case, motion in any direction is inhibited, which gives this effect the name *optical molasses.*

Changing the sign of δ also reverses the direction of the force. This is called "blue molasses" and atoms around $v = 0$ are accelerated.

Figure 1.1 indicates that the damping force vanishes for atoms with large velocities. The peak positions and heights depend on detuning and intensity. Increasing both parameters gives a larger "effective range" (capture velocity), but decreases the damping coefficient. Therefore, the capture velocity is defined as $v_c = \gamma/k$ for $s_0 \leq 1$ and $\delta = -\gamma/2$.

For atoms with very low velocities, the discrete absorption and emission steps need to be explored in more detail. Spontaneous emission leads to random momentum kicks on the atoms. This can be described as diffusion in momentum space, competing with the cooling effect of optical molasses. The resulting limit of conventional laser cooling is called *Doppler limit* and the associated Doppler temperature T_D is given by:

$$k_B T_D = \frac{\hbar\gamma}{2} \tag{1.10}$$

which is typically several hundred μK [10].

1.1.4 Cooling of Multi-Level Atoms

The model of laser cooling can be extended to multi-level atoms in a monochromatic light field. This makes cooling below the Doppler limit possible. Many different methods like polarization gradient cooling or velocity selective coherent population trapping have been developed during many years of research. This is a different branch of laser cooling than the one relevant for this thesis and only briefly mentioned here. Details can be found in [7] and the references therein.

1.1.5 Dipole Force

The radiative force and optical molasses are limited in magnitude by atomic parameters, such as the linewidth γ. Hence, it is not possible to increase the force arbitrarily by laser parameters. This is different for the dipole force, which results from a spatially varying light shift. The light shift for the ground state is given by [7]:

$$\Delta E_g = \frac{\hbar\Omega^2}{4\delta} \qquad \text{if} \qquad \Omega \ll |\delta| \tag{1.11}$$

$$\Delta E_g = \text{sgn}(\delta)\frac{\hbar\Omega}{2} \qquad \text{if} \qquad \Omega \gg |\delta| \tag{1.12}$$

with the Rabi frequency Ω (see also 1.2.1). The Rabi frequency is proportional to the magnitude of the electric field and therefore dependent on intensity.

In the case of a standing wave (optical lattice), the intensity and the light shift varies in space as $\cos^2(\mathbf{kx})$. This forms a potential and the spatial derivative gives the force on an atom. This force is analogous to the force on a classical dipole in an inhomogeneous electric field and therefore called dipole force. Unlike the radiative force, it does not saturate for high intensities. The direction of the force is determined by the detuning δ. Depending on its sign, atoms are attracted to the nodes or antinodes of the optical lattice.

Since the sign of the dipole force changes on the order of the wavelength, its average over longer distances vanishes. That prevents it from being a useful tool for atomic beam deceleration or collimation. However, optical lattices have many applications in AMO physics. For atomic nanofabrication, their use as non-physical masks is most important. Additionally, the theory for the bichromatic force was developed on basis of an extended dipole force scheme.

Another important difference from optical molasses is the conservation of energy in the case of the dipole force. This limits its application for laser cooling, since conservative forces can not change the phase space density of an atomic sample (Liouville's theorem).

1.2 Bichromatic Force

In the beginning of the studies of laser cooling, the picture of the two-level atom in a monochromatic light field was sufficient to describe the observed atomic behavior. Later, the model of a multi-level atom was required to explain detected experimental effects, which have been thoroughly studied for many years On the other hand, forces on a two-level atom in a multi-frequency light field was given less attention. Recently, the case of two-frequency light has been explored at Stony Brook. This *bichromatic force* has different properties than "classical" light forces and its application for atomic beam collimation is discussed in this chapter.

As mentioned in the previous section, monochromatic forces on atoms are either limited by atomic parameters or vanish in the average over several wavelengths. The reason in the former case lies in the spontaneous emission process. In contrast, stimulated emission makes it possible to control the direction of momentum exchange and also overcomes the limitation due to finite lifetime of the excited state. This enables coherent momentum exchange and a huge force which, unlike the case of the radiative force, does not saturate for high intensities.

1.2.1 Rabi Oscillations

To discuss the bichromatic force, it is first important to analyze the effect of monochromatic light on an atom in more detail. The probability for a two level atom to be in the excited state oscillates in time (spontaneous emsission is not considered here), depending on the intensity and the frequency of the light field. The probability $P_2(t)$ to be in the excited state is described by [8]:

$$P_2(t) = \frac{1}{2}\left(\frac{\chi}{\Omega}\right)^2 [1 - \cos(\Omega t)] \tag{1.13}$$

Ω is called *Rabi frequency.* In the case of a resonant light field, Ω is equal to the resonance Rabi frequency χ.

$$\chi = \frac{eE_0}{\hbar} \langle e|r|g\rangle \tag{1.14}$$

$$\Omega = \sqrt{\chi^2 + \delta^2} \tag{1.15}$$

This is illustrated for several parameters in figure 1.2. The Rabi frequency increases with intensity and detuning from resonance. A finite detuning also reduces the amplitude of P_2.

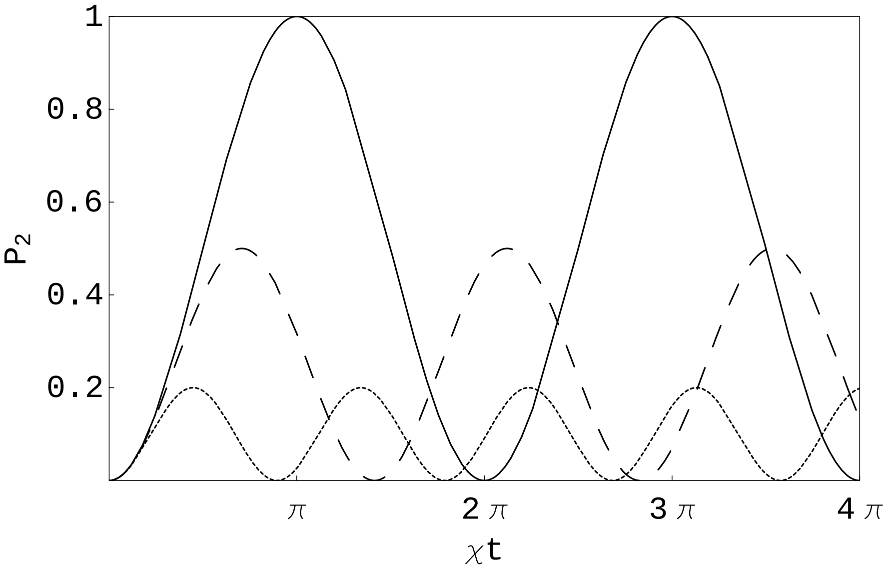

Figure 1.2 Probability P_2 as a function of time for different values of δ. solid line: $\delta = 0$, dashed line: $\delta = \chi$, pointed line: $\delta = 2\chi$

In the case of a resonant light field and the atom starting in the ground state, the excited state is reached after $t = \frac{2\pi}{2\Omega}$ with a probability of 1. Hence, a pulse of this length can drive the atom from the ground state to the excited state (or the other way). This time corresponds to a phase of π in the Rabi model and is therefore called π-pulse.

1.2.2 π-Pulse Model

The light field for the bichromatic force is formed by two frequencies of equal magnitude, detuned from atomic resonance ω_a by $\pm\delta$. These frequencies can be viewed as an amplitude modulated carrier wave:

$$
\begin{aligned}
E_{bichro} &= E\cos((\omega_a - \delta)t) + E\cos((\omega_a + \delta)t) \\
&= 2E\cos(\omega_a t)\cos(\delta t) \qquad (1.16)
\end{aligned}
$$

with ω_a as the carrier frequency, which is equal to the atomic transition frequency.

The amplitude of the electric field and therefore the rabi frequency oscillates with the detuning δ. If each frequency component gives a Rabi-frequency of Ω, then the (time-dependent) Rabi frequency of an atom in the bichromatic beam is given by (note: $\Omega = \chi$):

$$\Omega_{total} = 2\Omega\cos(\delta t) \qquad (1.17)$$

The overall intensity, which is determined by E in (1.16) is adjusted that each pulse of length $\frac{2\pi}{2\delta}$ forms a π-pulse. The condition therefore is:

$$
\begin{aligned}
\int_{-\pi/2\delta}^{\pi/2\delta} 2\Omega\cos(\delta t)dt &= \pi \qquad (1.18) \\
\rightarrow \Omega &= \frac{\pi\delta}{4} \qquad (1.19)
\end{aligned}
$$

To get an effective force, two counterpropagating bichromatic beams are necessary. One of these beams excites the target atoms, the other one deexcites them by π-pulses. Since their $\mathbf{k}$-vectors are antiparallel, both give a momentum transfer of $\hbar\mathbf{k}$ (same direction!). The time for this process is given by the length of one π-pulse, resulting in a first estimate of the bichromatic force:

$$F_{bichro} = \frac{2\hbar k\delta}{\pi} \tag{1.20}$$

To transfer momentum coherently between light field and atoms, the relative phase of both counterpropagating beams has to be adjusted (see figure 1.3).

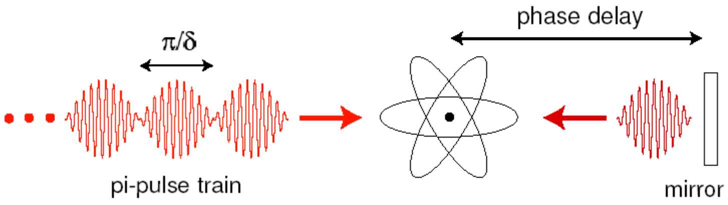

Figure 1.3 The π-pulse model of the bichromatic force describes excitation and deexcitation of atoms by counterpropagating beams. The mirror position defines the phase delay, which affects the direction of the resulting force.

Since temporal overlap of two pulses is not desirable, a phase delay of π seems to be a good choice. However, taking spontaneous emission into account changes this picture. Spontaneous emission will bring an atom to the ground state, when it is supposed to be in the excited state. The next π-pulse, which should deexcite the atom, will excite it. This reverses the direction of the resulting force, until the next spontaneous emission occurs. Therefore, the average of the force over several atomic lifetimes vanishes.

To overcome this, an asymmetric timing of the pulses is used. The atoms should spend less time in the excited state than in the ground state. The optimum phase delay was determined numerically to be $\sim \frac{\pi}{2}$ (see 1.2.3). Thus, the atom spends 1/4 of one cycle in the excited state and 3/4 in the ground state. A spontaneous emission process will exchange this, leading to the atom spending long time in the excited state. There it will undergo another spontaneous emission with higher probability. In a long time average, the atom spends 1/4 of its time in the "wrong cycle", where the direction of the force is reversed and 3/4 in the desired cycle, affected by the full bichromatic force. This reduces the estimate of the bichromatic force of (1.20) to half of its value:

$$F_{bichro} = \frac{\hbar k \delta}{\pi} \tag{1.21}$$

F_{bichro} scales with the laser parameter δ. This is typically much larger than the linewidth γ, leading to a huge force, compared to optical molasses ($F_{OM} \simeq \frac{\hbar k \gamma}{2}$).

The π-pulse model offers an intuitive description of the bichromatic force and gives a the value of several parameters as well as an estimate of its magnitude. However, several issues are not addressed. For example, the temporal overlap of two pulses is not considered. There is also a dressed-atom model to describe the bichromatic force, which leads to the same result for the magnitude but gives a slightly different relation between Rabi frequency and detuning (analogous to (1.19)). Nevertheless, a theory giving good quantitative results, especially for velocity dependence, has not been developed yet.

1.2.3 Bichromatic Force Simulation

The lack of quantitative predictions of a force profile makes a simulation of the bichromatic force necessary. The simulation uses a Fortran code and is based on the numerical integration of the optical Bloch equations. It was originally developed by R. Grimm et. al. [17] and is described in detail in [1, 5]. It gives the bichromatic force profile as a function of atomic velocity. The input parameters are detuning δ, Rabi frequency Ω (both in units of γ) and phase delay. One of these force profiles is shown in figure 1.4.

The result of the simulation shows the extraordinary features of the bichromatic force. Its magnitude is much higher than optical molasses, and also the capture range lies beyond the limits of traditional forces. The force profile is nearly constant over a wide range and drops of fast at the edges. The peaks in the profile are partly numerical artifacts and partly multiphoton effects (Dopplerons) [11].

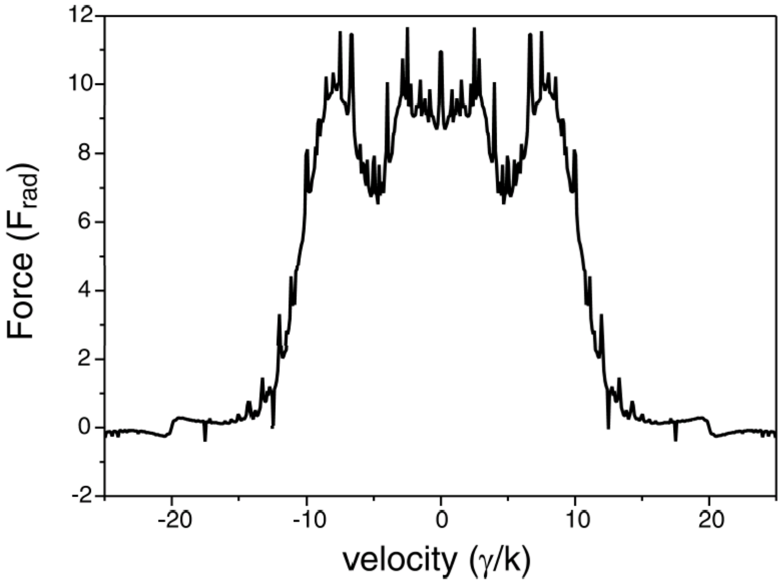

Figure 1.4 Bichromatic force profile simulated by the Fortran code mentioned in the text. The parameters for this plot are $\delta = 20\gamma$, $\Omega = 22\gamma$, $\phi = \frac{\pi}{2}$.

1.2.4 Bichromatic Collimation

The unmodified profile of the bichromatic force (figure 1.4) is only of limited use for collimation purposes. For collimation, the force should vanish at $v = 0$ and have a strong velocity dependence around this point. Therefore, the force profile is shifted along the velocity axis by Doppler-detuning the laser beams and a second profile with reversed sign and which affects atoms moving in the opposite direction is added. The resulting force profile is given in figure 1.5. It shows the desired behavior with $F_{bichro} = 0$ at $v = 0$ and $\frac{\partial F}{\partial v} < 0$ around that point.

The experimental realization of the second force profile is not as straight-

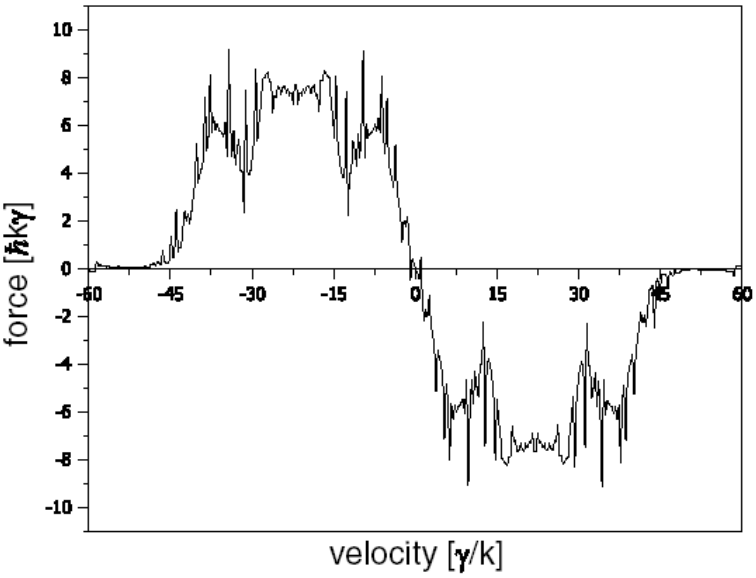

Figure 1.5 Force profile for bichromatic collimation. The parameters are equal to those in the actual experiment ($\Omega = 41\gamma$, $\delta = 37\gamma$, $\Phi = \frac{\pi}{2}$)

forward as in the case of optical molasses. Overlapping all four beams in the same interaction would violate the phase condition for bichromatic collimation and is therefore not possible. Instead, two spatially separated interaction regions are required for collimation in one dimension. Each acts on atoms with either positive or negative velocity along the collimation direction. The combination gives the profile of 1.5.

The force profiles are shifted along the velocity axis by Doppler-detuning and therefore moving the center to $v \neq 0$. Since the **k**-vectors of both beams are antiparallel, one of them needs to be blue detuned and the other one red. This leads to different frequencies in the two beams and bichromatic collimation can not be illustrated by the simple retro-reflection scheme of figure 1.3. In the experiment, each beam carries the name of its Doppler detuning ($+kv$ and $-kv$).

Hence, bichromatic collimation requires light of four frequencies in two beams. This frequencies are illustrated relative to atomic resonance in figure 1.6.

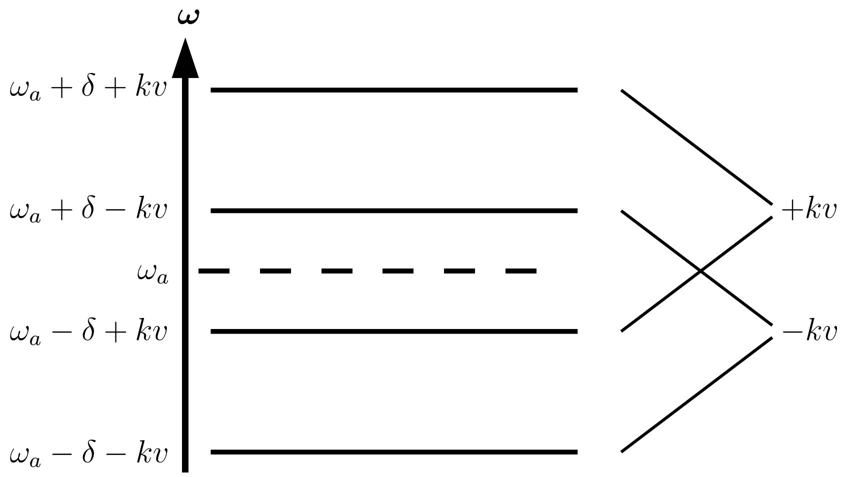

Figure 1.6 Frequencies for bichromatic collimation relative to the atomic transition frequency ω_a.

This Doppler detuning explains why the bichromatic force is dissipative, even without spontaneous emission. In the π-pulse model, the excitation is always done by the $-kv$ and the deexcitation by the $+kv$ beam. Therefore, the atom looses $|2\hbar kv|$ kinetic energy during one absorption-emission cycle.

1.3 Atomic Nanofabrication

Current lithography processes use ultraviolet light or electron beams, but these methods are reaching their fundamental limit. In the case of ultraviolet light, the minimum structure size is on the order of the wavelength and limited by diffraction. Electron beams offer adjustable de-Broglie wavelength, but electrons of high energy (and therefore short de-Broglie wavelength) undergo multiple scattering inside the resist layer. This leads to broadening of structures and limits the resolution of this method. In addition, beams of charged particles can only be focused to a certain extent.

Using neutral atoms can overcome these limitations. Due to their higher mass, atoms have a small de-Broglie wavelength, even at low energy. The atomic structure allows manipulation of their motion by using laser beams. This makes beam collimation possible and physical masks are not necessary, since atoms can be guided microscopically by optical light masks. This field is called *atomic nanofabrication* [22].

Today, there are two main branches of atomic nanofabrication, *direct deposition* and *neutral atom lithography.* Both methods use neutral atomic beams, but patterns are created in a different way. Whereas the latter technique is the main concern of this thesis, it is worth mentioning the former. In direct deposition, structures are created out of the atoms forming the beam. Typically, a light mask is used to guide atoms to certain points on a wafer where they accumulate and grow structures. The atomic beams are usually formed by high temperature evaporation of metals (sodium, chromium, aluminum). The use of non-physical masks usually requires low beam divergence, which makes beam collimation necessary. Therefore, atomic transitions must be accessible with standard laser sources. Additionally, direct deposition requires a high dose of atoms (many monolayers) to create structure heights of technological interest.

On the other hand, neutral atom lithography (NAL) is a two-step process, similar to optical lithography. Here, a thin (organic) resist layer is used on the surface of the sample. The atomic beam is usually formed by metastable rare gas atoms, which carry high internal energy in a state of long lifetime. This energy is released at collision with the sample, which damages the resist layer. This chemical surface modification is transferred to the substrate by etching, which makes theoretically background free structures possible. The resist layers are typically very thin (monolayers) and only a low dose of atoms ($<$ 1 monolayer) is necessary in the exposure, which shortens the exposure time. NAL is possible with a wide variety of substrates and resist layers. In most cases, the atomic beam is formed by metastable noble gases. The respective transitions are well studied and laser sources are available.

Metastable Helium

Metastable helium (He*) carries the highest internal energy of all metastable noble gas atoms (19.8 eV). The effective ground state is 2^3S_1 whose decay to 2^1S_0 is forbidden by several selection rules. This leads to a very long lifetime (∼8000 s). From this metastable ground state, the atom can be further excited to 2^3P_2 by light of 1083 nm wavelength. These two states form the effective two-level atom for interaction with light. Another transition ($2^3S_1$to 2^3P_1) lies ∼2.3 GHz higher (figure 1.7) and only plays a role in the case of high blue laser detuning. The properties of this transition can be found in table 1.1. Note the low saturation intensity. This makes a high saturation parameter accessible with modest laser power. The spin of the ^{4}He nucleus is 0 and therefore the spectrum shows no hyperfine structure.

λ/nm (vacuum)	$\hbar\omega_a$/eV	$\frac{\gamma}{2\pi}$/MHz	$s/\frac{mW}{cm^2}$
1083.33	1.144	1.62	0.17

Table 1.1 Several properties of the $2^3S_1 - 2^3P_2$ transition in helium, from [7].

Metastable rare gas atoms are commonly created in an electric discharge and have thermal kinetic energies, giving de-Broglie wavelengths on the order of angstroms. This pushes the fundamental diffraction limit of this method to the size of an atom. Collisions quench metastable atoms immediately and leave an inert atom, which results in localized energy deposition on the sample.

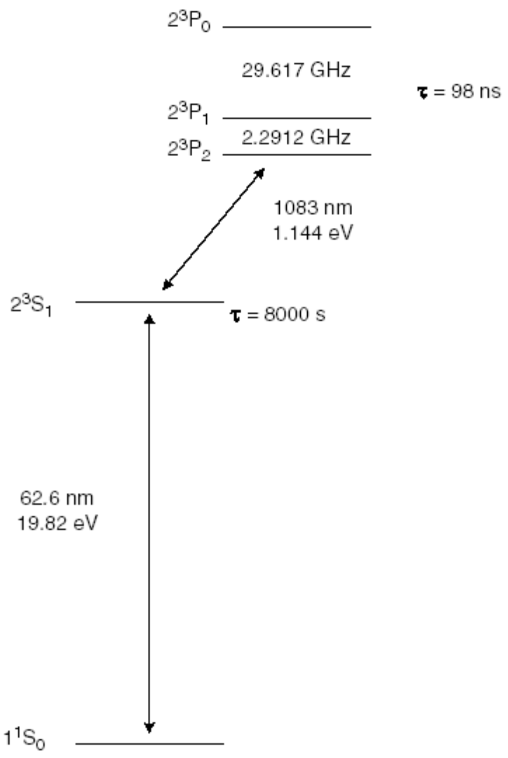

Figure 1.7 Diagram of experimentally relevant levels in helium. 2^3S_1 is the effective ground state for the metastable atom, whereas 1^1S_0 is the real ground state of He. Note that the energy levels are not drawn to scale.

The internal structure allows beam manipulation by light forces. Unlike beams of charged particles, no internal forces cause beam distortions which lead to a lower resolution.

In the actual experiment, a self-assembled monolayer (SAM) of nonanethiol or dodecanethiol is used as resist on the sample. Exposing this layer to metastable helium atoms damages these organic molecules and changes the local wetting properties on the surface. This allows a water-based etching solution to attack the gold layer on the substrate, transferring the pattern on the SAM permanently into the surface (see 4). Several experiments [29, 30] showed, that a small dose of about one He^* atom per SAM molecule is enough to get good contrast in the etching process. However, the efficiency in the production of metastable helium is low, which leads to low intensities in the atomic beam. The output of the source can not be strongly increased by external parameters (see 2.1). This leaves beam collimation as a promising method to reach shorter exposure times. Additionally, beam collimation is desirable to achieve low beam divergence which reduces abberations. For the work of this thesis, the methods of atomic beam collimation by bichromatic light and neutral atom lithography are combined for the first time.

Many neutral atom lithography experiments have been done using gold coated silicon samples with alkanethiol resist, mechanical masks and atomic beams of metastable rare gas atoms. The first results were published in 1995 by Berggren et al. [23] using metastable argon and helium [24], which showed a resolution of ∼100 nm. Other groups publish lower resolution down to 40 nm [26, 29].

There are several variations of these "standard materials". For example, cesium [27] has been used to pattern alkanethiol SAMs. It was also found that dilute hydrocarbon vapor (diffusion pump oil) can form a resist layer which is sensitive to the exposure of metastable noble gas atoms and can be used as "contamination resist" in lithography experiments [28]. Since the roughness of gold layers on silicon is high, other groups tried to get a smooth gold coating by using muscovite mica as substrate [31, 32].

In all these experiments, the structures are etched into a gold layer and its thickness determines the structure height. This height is usually 20 to 30 nm. The use of thicker gold layers is limited because the etching of gold is isotropic and the obtainable resolution depends on this value. However, the gold pattern can be used as a mask for anisotropic plasma etching of silicon, giving structures of several hundred nm height [25].

Light masks are commonly used in atomic nanofabrication, especially in direct deposition methods. Petra et al. [6, 30] used a high-power light mask (1D and 2D) in combination with a atomic beam of metastable helium. In contrast to the experiments using metastable rare gas atoms mentioned above, the atomic beam was collimated by optical molasses. The collimation not only enables shorter exposure times, it also reduces abberations of a light mask. For the near future, experiments with a collimated beam (as described in this thesis) and a low-power mask are planed in the laboratory at Stony Brook.

Chapter 2

Vacuum System

The beam of metastable helium is produced and collimated in a high vacuum system (base pressure 6×10^{-7} torr). This system also houses several detectors to characterize the atomic beam. Its end part can be separated by a gate valve and is used as a loading chamber for the exposure of lithography samples.

2.1 Metastable Helium Source

The metastable helium source in the experiment works with a plasma produced by a DC electric discharge. It uses the "reverse flow" design [19] and produces a relatively high output of metastable atoms. It consists of a stainless steel jacket with 3 cm inner diameter (see figure 2.1). This jacket is cooled by liquid nitrogen. Inside is a pyrex glass tube of 1 cm diameter with a narrowed end. This tube is held centered in the jacket by a teflon spacer. In the center of the tube is a needle (1 mm diameter) with a tungsten tip. A ceramic spacer keeps the needle centered in the glass tube. The needle is connected to a linear motion feedthrough which allows motion along its axis to adjust the discharge distance. On the front end, an aluminum plate with a 0.5 mm diameter hole (nozzle plate) separates this inner source region from the rest of the system. In front of the nozzle plate is the skimmer whose aperture has also a diameter of 0.5 mm. The skimmer connects the source to the beam chamber.

Helium enters the source on the outside of the glass tube, where it is in thermal contact with the liquid nitrogen cooled jacket. The back end of the glass tube is connected to a mechanical pump, which pumps out most of the helium. A negative high voltage is applied to the needle, which powers a glow discharge between the needle tip and the nozzle plate. In this discharge, metastable helium atoms are produced by electron impact. However, most of these are quenched by collisions. On the edge of the plasma and the afterglow between nozzle and skimmer, where the particle density is lower, the produced metastables have a higher survival probability and can enter the vacuum system through the skimmer. A viewport allows watching the discharge in front of the nozzle plate. This enables us to detect contaminations in the supplied helium or inside the glass tube, which lead to an easily observable change in discharge color and brightness.

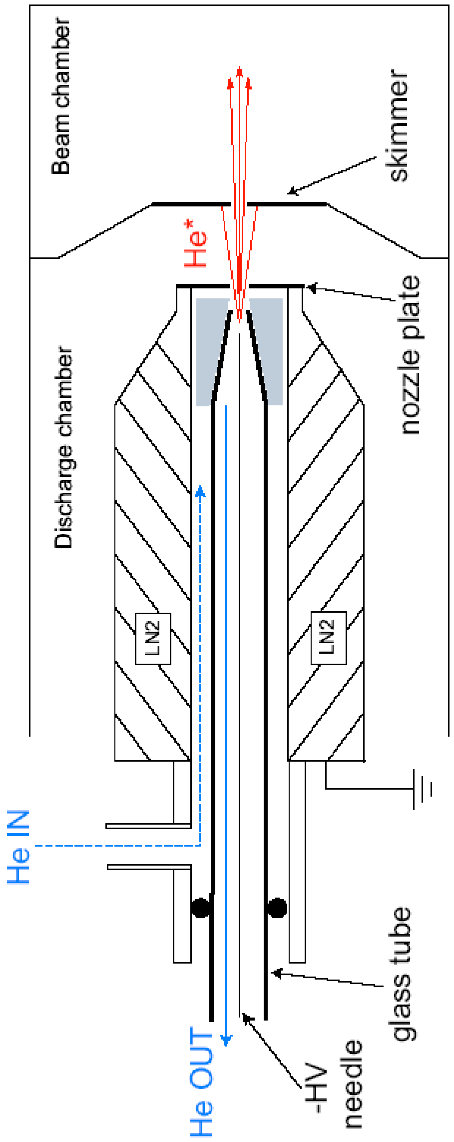

Figure 2.1 Drawing of the metastable helium source. The viewport (not shown) allows us to look at the region between nozzle and skimmer. The ceramic spacer which centers the needle in the glass tube is also not shown.

The main component of the produced atomic beam is neutral (singlet) helium. Only one out of 10^4 to 10^5 [2] atoms is in the metastable (triplet) state. The beam also contains electrons and charged helium atoms. The discharge emits light in the visible and ultraviolet range. Especially ultraviolet light and charged particles produce the same signal as He^* and they also damage the SAM on lithography samples. These effects are discussed in Chapter 5.

To maintain high vacuum conditions in the beam chamber during operation (when helium is flowing through the source), the vacuum system is differentially pumped by two Pfeiffer TPH 330 turbo pumps (pumping speed 330 $\frac{l}{s}$). The pressure in source and beam chamber is measured by two Kurt J. Lesker G100F ion gauges. During operation of the source, the pressure in the source chamber rises from its base value of 2×10^{-6} torr to 1.2×10^{-4} torr. The beam chamber is affected to a smaller extend and the pressure rises only from 6×10^{-7} torr to 4×10^{-6} torr.

The operation of the source depends on the parameters discharge current, helium pressure and the position of the needle tip. Low pressure reduces collisional quenching and therefore enhances the production of He^*, but also makes the discharge less stable. Two Granville-Phillips Convectron gauges measure the helium pressure on the inlet and the outlet of the source. A needle valve is used to adjust this pressure. The inlet pressure was typically between 5 and 10 torr, where the outlet pressure was kept at 1.2 torr.

A high voltage of typically –2100 V is necessary to run the discharge. The current is limited by a ballast resistor and can also be adjusted by the power supply. The experiments presented here were done at 6 mA. Both higher and lower currents lead to unstable source operation. Higher currents are known to produce more metastable atoms [2], but also reduce the lifetime of the source. In addition, higher currents make the discharge "hotter" and the longitudinal velocity slightly larger [1], leading to less effective collimation.

The position of the needle is adjusted while running the collimation beams and measuring the peak flux of He^* with a stainless steel detector (see 2.4.2). The position of the needle has only a small effect on the efficiency of the source, but it is important for the stability of the discharge.

The longitudinal velocity distribution was measured by M. Cashen [1] using a time of flight method. The cooling of the source with liquid nitrogen shows a significant effect. It reduces the peak velocity to $\sim 1000\ \frac{m}{s}$, whereas it is around 2500 $\frac{m}{s}$ at room temperature [4]. A source of similar design, cooled by liquid helium, shows a even lower velocity of $\sim$300 $\frac{m}{s}$ [15]. The velocity FWHM at liquid nitrogen temperature is 400 $\frac{m}{s}$ [1].

2.2 Beamline

The central part of the vacuum system (beamline) is designed to allow collimation of the atomic beam as well as its detection. It is a stainless steel tube of 4" diameter and a length of 40 cm with several side ports. All connections are copper sealed Conflat, which support very low (UHV) pressure.

A 6" six-way-cross was directly welded to the source to allow optical access to the atomic beam directly after the skimmer. This gives the possibility to effectively collimate the atomic beam before it expands too far. Four ends of this six-way-cross are flanged by windows with an open diameter of 4". These windows are coated to have high transmission for light of 1083 and 389 nm. The second wavelength marks the 2^3S_1–3^3P_2 transition in helium, which is not used in the experiments described here.

To avoid Zeeman shifts of atomic energy levels, which might bring atoms out of resonance to the laser, the magnetic field present in the lab needs to be canceled in the interaction region. The geometry of the system does not allow the use of Helmholtz coils, so we use coils of different diameter and number of turns. A simulation using a Mathematica code shows that they create a magnetic field which is constant within 1 % in the interaction region.

After this interaction region, two vertical stainless steel plates are placed in the system. They are connected to high voltage and the resulting field deflects

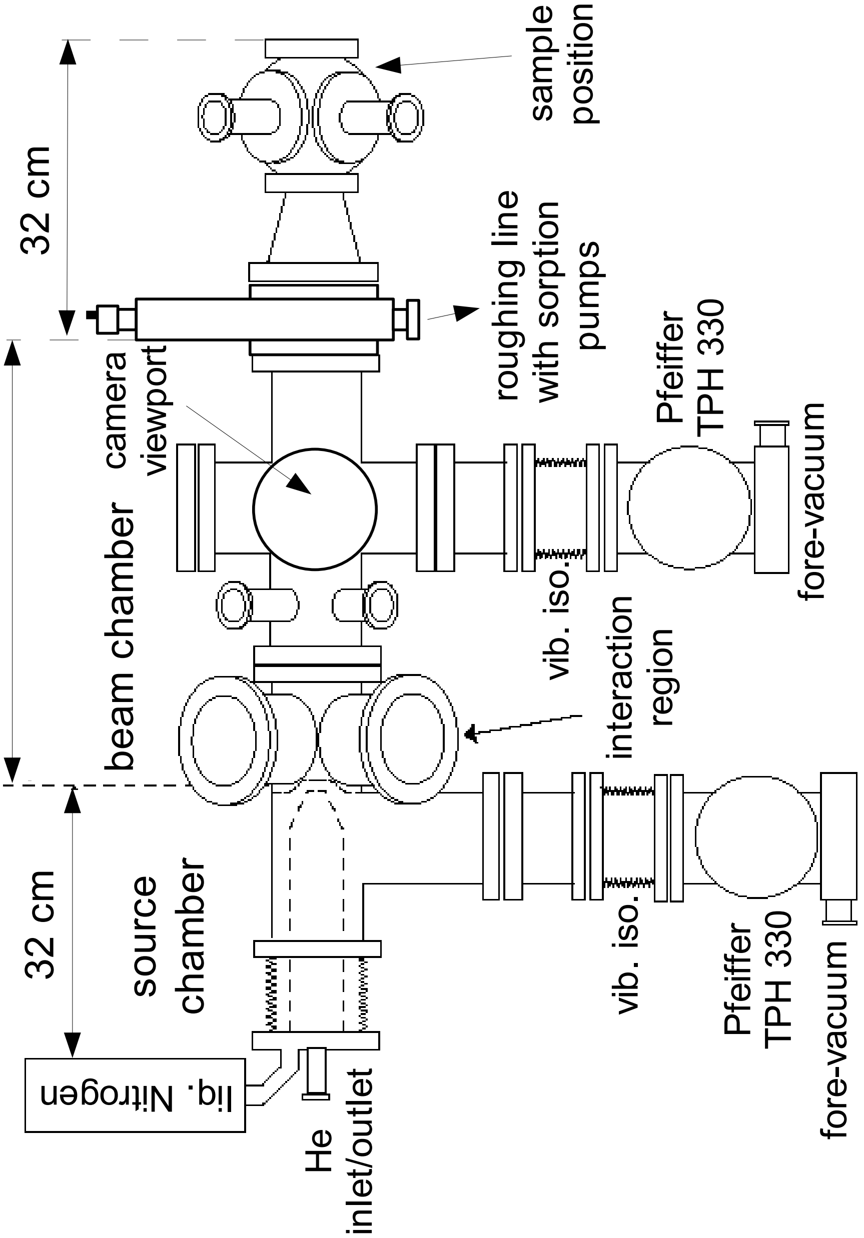

Figure 2.2 Vacuum system for neutral atom lithography. All connections are copper sealed Conflat, besides the source inlet/outlet (Kwik-Flange) and the flanges holding the two turbo pumps.

charged particles out of the atomic beam.

The next part further down the beamline is another 6” Conflat six-way cross. It has several smaller flanges (2 3/4” Conflat) for additional equipment. This part is aligned that it has two horizontal and two vertical 6” ports. The lower port is connected to the second turbo pump (see figure 2.2). The upper one supports a linear motion feedthrough, which holds a multichannel plate/phosphor screen detector together with a mirror (see 2.4.1). The feedthrough makes it possible, to have the detector variably in or out of the atomic beam. The mirror is mounted on an angle of 45° with respect to the phosphor screen, which makes it possible to watch the phosphor screen through a window on one of the horizontal flanges.

This part of the system also contains a stainless steel detector (SSD) which allows scans of the atomic beam close to the interaction region. Unfortunately, this detector is affected by noise and does not give conclusive data. For the lithography experiments, we are more interested in scans of the atomic beam close to the sample, which were provided by another SSD in the sample chamber.

2.3 Sample Loading Chamber

The end of the vacuum system can be separated by a Thermionics PFG-TLG-4000-H/R gate valve (4” inner diameter) and is used as loading chamber for lithography samples. The chamber itself consists of a 4 1/2” spherical cube (Kimball Physics MCF450-SC-60000-A), connected to the gate valve by a conical reducer. The spherical cube houses a special SSD (see 2.4.2), which allows 2D measurements of the atomic beam cross section.

The gate valve is connected to two cryogenic sorption pumps by a roughing line (all connections 2 3/4” Conflat). These pumps reduce the pressure in the loading chamber to $\sim$10 mtorr without risking hydrocarbon contamination of the system. The roughing line also contains a Convectron gauge and a venting valve, connected to a nitrogen tank in order to allow backfilling the system without contaminations of ambient air.

The sample holder consists of two home-made aluminum plates. The front plate has a circular aperture of 0.5” diameter. The sample and the mechanical mask are sandwiched between both plates with ceramic rods (Kimball Physics eV-parts). The back plate is connected to the spherical cube by a Kimball Physics Groove-Grabber system. The sample holder is electrically grounded. The mechanical mask is a copper TEM Grid (Electron Microscopy Sciences 79526-20) with 2000 wires per inch (2000 Mesh), which gives a periodicity of

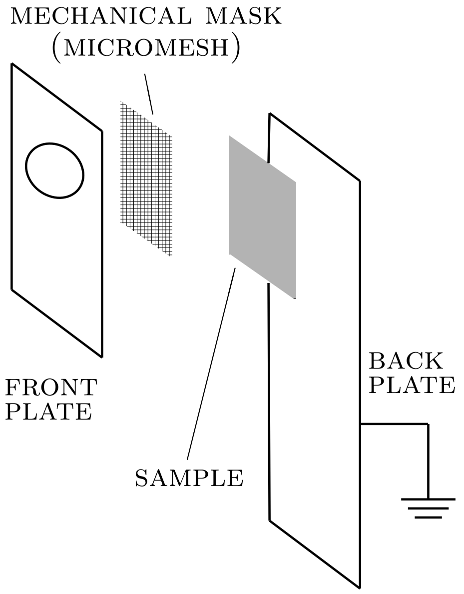

Figure 2.3 Sample holder for NAL. The mechanical mask and the sample are sandwiched between two aluminum plates. These two plates are connected by ceramic rods (not shown).

12.5 μm. The grid is held on the surface of the sample by the two aluminum plates.

2.4 He* Detection

The detection of metastable rare gas atoms relies on their high internal energy. This energy is released in collisions, causing ionization in the target material. The experimental setup contains two complementary detector schemes to determine the flux of He* in the atomic beam. A combination of a multichannel plate (MCP) and a phosphor screen is used for real-time, two-dimensional imaging detection, whereas a set of stainless steel detectors (SSD's) offers high linearity in the output signal.

2.4.1 MCP/Phosphor Screen

The multichannel plate/phosphor screen detector is 22 cm away from the skimmer and allows real-time imaging of the atomic beam. The whole assembly of this detector is shown in figure 2.4.

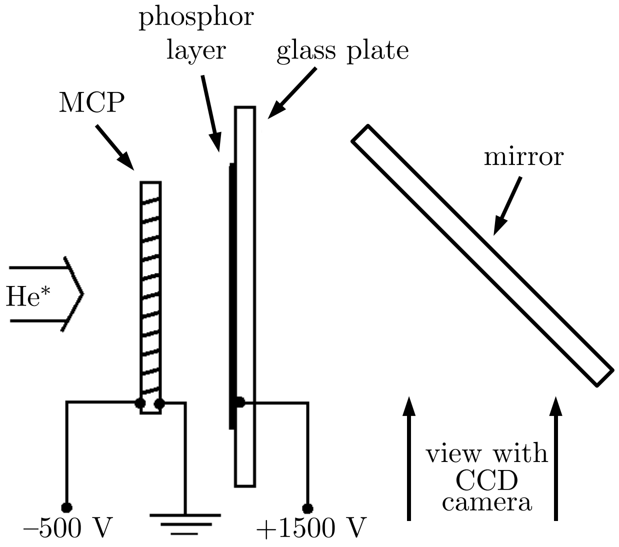

Figure 2.4 Top view on multichannel plate/phosphor screen detector. The camera detects the phosphor screen through a window on one of the horizontal flanges of the vacuum system. Typical values for applied voltages are shown

The three detector parts (MCP, phosphor screen, mirror) are put together by Kimball Physics eV-parts. This set is mounted to a linear motion feedthrough, which makes it possible to retract it out of the atomic beam.

The MCP (Burle) has an active diameter of 25 mm and contains a large number of channels (10 μm diameter) on a hexagonal grid with periodicity of 12 μm. A negative high voltage, typically 500 V, is applied to the front side whereas the back side is grounded. He* atoms hitting the front side release electrons from the inside of the channels. These are accelerated inside the channels and release more electrons by electron-wall collisions. The total amplification factor of the MCP can be adjusted up to $\sim 10^3$ by the applied voltage (up to 1000 V).

The second part of this detector is a phosphor screen (manufactured by James van House, Vancouver, WA). It consists of a glass plate that is coated with a thin, transparent gold layer for conductivity and a layer of phosphor. A positive high voltage (around 1500 V) is applied to the gold layer. The resulting electric field accelerates electrons emitted by the MCP to the phosphor layer, where they excite phosphor atoms. We detect fluorescent dexcitation, which occurs around 450 nm, with a CCD-camera.

This camera is mounted outside the vacuum system and detects the phosphor screen image through a window on one of the side flanges of the six-way cross (see figure 2.2). It is connected to a computer by a TV tuner card. This system is used for both real time observation and to take bitmap pictures for further analysis. The high speed of this detector is very useful for alignment purposes.

Unfortunately, this detector gives only qualitative results. The reasons for that are manifold. The linearity of both MCP and phosphor screen with the flux of He^* respectively electrons is limited. Whereas this can in principle be solved by measuring a calibration curve, the phosphor screen also shows aging effects. This leads to inhomogeneous (exposure history dependent) and time dependent gain of the system. Therefore, another detector scheme is used to get quantitative measurements.

2.4.2 Stainless Steel Detectors

The experimental setup contains two home-built stainless steel detectors, which work similar to a Faraday cup. A front plate with an aperture geometrically defines a part of the atomic beam to measure. Metastable helium atoms, which pass this aperture, hit a stainless steel back plate. At the collision, the internal energy is released and extracts electrons out of the back plate with a high efficiency of 70 % [16]. These are collected by the front plate, which is kept at +250 V. The back plate is connected to ground through a Keithley 486 picoammeter. The measured current is directly proportional to the flux of metastable helium integrated over the area of the aperture. The whole detector is movable and can be scanned perpendicular to the atomic beam.

The system contains two stainless steel detectors, one 16 cm away from the skimmer with a circular aperture, and a set of crossed slits 48 cm further down the atomic beam (64 cm from skimmer). Unfortunately, the first detector is strongly affected by noise and background (see below) and does not give conclusive data, despite the attempts to control these undesired effects. On the other hand, the set of crossed slits give highly repeatable results. This second detector has two front plates (see figure 2.5) which each have a long rectangular slit instead of a circular aperture. They are connected to independent feedthroughs, which move perpendicularly. This allows two-dimensional scans of the atomic beam profile. The scan range is 1 cm on the first and 4.25 cm on the second slit. This detector is close (4.5 cm) to the sample holder and used to determine the exposure dose in the lithography experiments.

There are different sources of noise and background which affect the stainless steel detectors. Besides atoms in a metastable state, the output of the source also contains charged particles (mainly He^+ and electrons), visible and UV light. The current due to charged particles was found to fluctuate strongly in time as well as in detector position. This problem could be solved by applying high voltage (–1000 V) to the deflection plates. This voltage has been chosen to minimize negative background contributions in the detected signal [3].

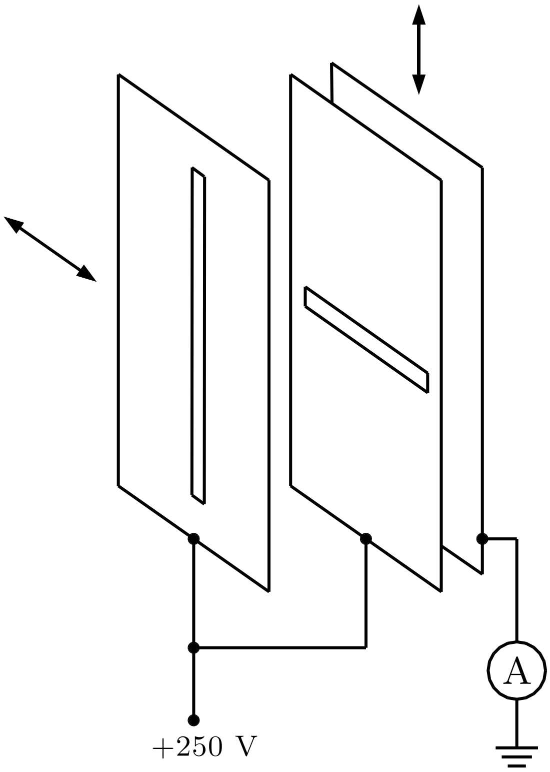

Figure 2.5 Principle of the stainless steel detector with crossed slits as aperture. The signal is produced by He* atoms passing both slits and ejecting electrons of the back plate. The arrows indicate the direction in which the slits could be moved.

In addition, we use magnetic fields to deflect charged particles. However, they can not be used near the interaction region since stray fields may affect the atoms there. A strong permanent magnet (magnetic optics mount) was installed on the conical reducer between gate valve and spherical cube (see figure 2.2). After that improvement, the signal on the back SSD was almost free of noise.

However, the remaining background (no collimation lasers active) signal is not only due to metastable atoms, but is constant in time. Therefore, it could be quantified before the actual experiment by deflecting metastable helium atoms with “blue molasses”. The signal analysis is described in detail in section 5.1.2.

Chapter 3

Laser System

Bichromatic collimation needs light of four frequencies with high power. The required intensity scales as δ^2, giving $s \sim 4000$ for the settings in our experiment. In addition, another optical molasses stage was used for further collimation, requiring another frequency near atomic resonance. The devices to create the desired light are concern of this chapter. The whole laser setup and the relative optical frequencies are shown in figure 3.1.

3.1 Light Production

The light for the experiment is produced by a Spectra Diode Labs SDL-6702-H1 Distributed Bragg Reflector (DBR) laser diode with an extended cavity. This diode has been in use since 1999 and served as light source for previous experiments to study bichromatic forces on metastable helium atoms [12, 13, 14].

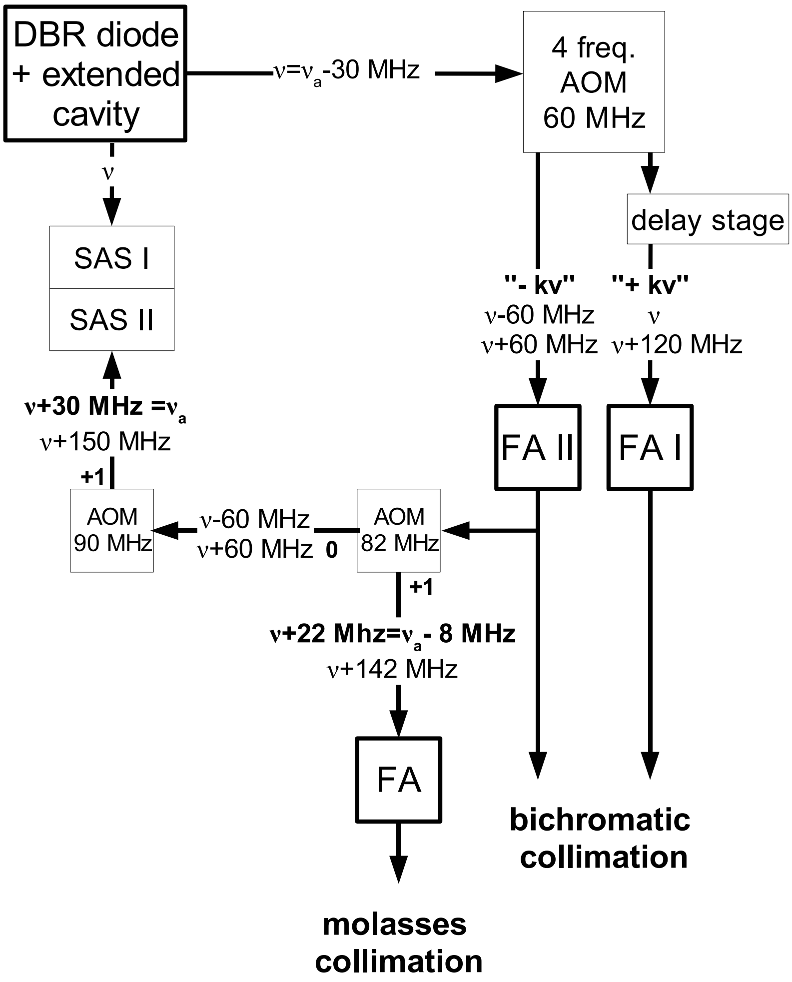

Figure 3.1 Laser setup for bichromatic and optical molasses collimation. The extended cavity offers two output beams at the laser frequency ν (figure 3.3). In the experiment, this frequency is detuned by 30 MHz from the atomic transition at ν_a. Each output beam of the four-frequency AOM (section 3.3) contains two spectral components (bichromatic light), which are also present in the molasses collimation beam. There, one component is close to resonance (bold font) and the effect of the other can be neglected. Both frequencies are detected by the saturated absorption spectroscopy setup (SAS II). One of them is used to lock the laser (section 3.2) and therefore equal to the transition frequency. SAS I is used to check the laser output. The numbers on the AOMs indicate the diffraction order.

This type of laser diode has a diffraction grating located on the diode itself which serves as a frequency selector. Therefore, the output of the diode is relatively narrow-band. The emission wavelength is at 1083 nm, but the exact value depends on temperature and input current. The linewidth of the free-running diode was determined to be ∼3 MHz [1].

In the experimental setup, the diode is incorporated in an extended cavity (see figure 3.3) which gives optical feedback into the diode. The length of this extended cavity also affects the emitted frequency.

The effects of the different diode parameters on the output power and wavelength are discussed below.

Temperature

The diode temperature affects the refractive index as well as the physical length of the diode, thus changing the optical cavitylength and therefore the spectral position of cavity modes. The diode includes a temperature sensor and a thermoelectric cooler. A ILX Lightwave LDT-5910 temperature controller is used to keep the temperature constant at 24.4 °C.

It was necessary to change this setting sometimes to have the laser running stable on the desired frequency. This can be due to aging effects, since the diode has been used for polychromatic force experiments since 1999.

Input Current

The diode current affects the output power as well as the output frequency. The nominal output power is 50 mW at a current of 170 mA. In order to reach the desired frequency near atomic resonance, the diode is used at a lower injection current of ∼140 mA, provided by a ThorLabs LDC 500 laser diode driver. The output power as a function of injection current is shown in figure 3.2. Note that measured power is lower than the actual output because this measurement has been done using the 70 %–output (see figure 3.3).

To bring the laser to the desired frequency, the diode current is set so that the absorption peaks could be seen on the SAS signal with an oscilloscope (the frequency was scanned by the extended cavity). The fine tuning is done by adjusting the length of the extended cavity.

The controller also allows modulation the diode current up to a frequency of 150 kHz by an analog BNC input. This is used to dither the frequency in order to lock the laser relative to the atomic transition (see section 3.2).

Extended Cavity

The beam emitted by the laser diode is split into a main output (70 %) and a feedback component by a beamsplitter. The arrangement is shown in figure 3.3. Since the feedback passes again the same beamsplitter, only 9 % of the

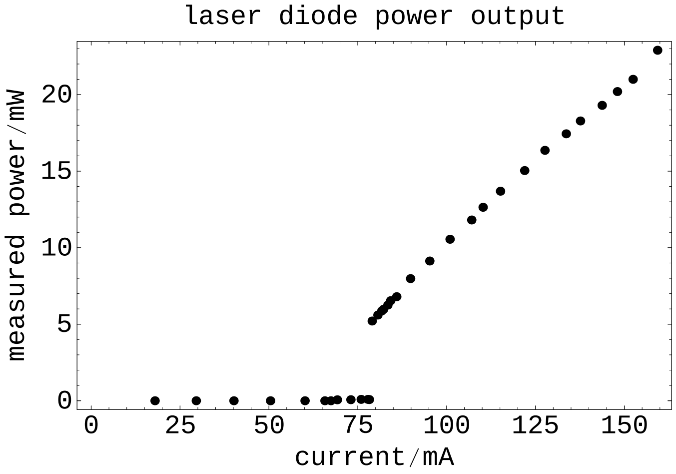

Figure 3.2 Output power of the laser diode over input current. The power was measured at the 'experiment' output of the extended cavity (see figure 3.3) and therefore around 70 % of the power out of the diode. Here, the diode temperature was set to 24.1 °C.

original output are reflected back into the diode and the remaining 21 % form a second output, which is used for saturated absorption spectroscopy (SAS).

The optical length of the extended cavity gives an additional mode condition and therefore affects the output frequency. This leads to the effect that the laser becomes very sensitive to any variations of the optical cavity length, like vibrations or air currents. To limit these, the whole extended cavity is on a massive block of aluminum inside a box of insulating material (polystyrene foam).

To change the length of the extended cavity for frequency modification, the reflecting mirror is mounted on a piezo-electric transducer (PZT). This device

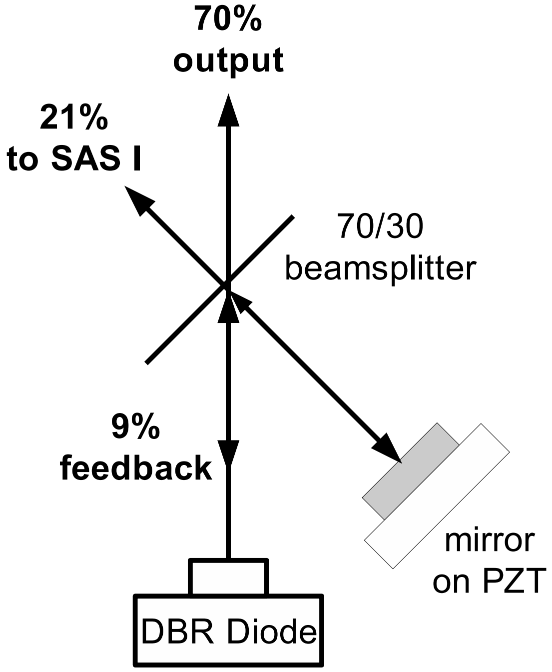

Figure 3.3 Laser diode in extended cavity. The cavity is created by a beamsplitter and a highly reflective mirror. The cavity length can be adjusted by a PZT. The strong output beam goes to the experiment, the secondary gives light for one of the SAS systems.

changes its length proportional to an applied voltage. A home-build high voltage amplifier is used to drive the PZT. By ramping the driving voltage, it is possible to scan the laser frequency over a range of ~100 MHz and detect absorption peaks on the SAS signal.

To lock the laser frequency to the atomic transition, an error signal is applied to the PZT to keep the laser on the desired absorption peak (see also section 3.2).

In the main output, an optical isolator (OFR IO-3-1083-HP) prevented reflections from the optical system back to the laser diode in order to avoid frequency instabilities. This is not the case for the secondary output, so that the SAS setup can give feedback to the laser (by forming another external cavity). Since the length of this cavity is not stabilized, the laser frequency can drift. This can be avoided by a slight 'misalignment' of the SAS, which does not effect its function but gives a reflected beam not exactly retroreflected on the incoming beam.

The extended cavity also reduces the linewidth of the laser. It was measured to be 125 kHz [1] by beating with a second laser of the same type. This is one order of magnitude lower than the natural linewidth of the relevant atomic transition ($\gamma = 2\pi \cdot 1.6$ MHz).

After the isolator, the light is coupled into a single mode fiber. The output of this fiber is single mode Gaussian, so the experiment is provided with spatially well defined beams.

3.2 Frequency Locking

The frequency of the light needs to stay constant relative to the atomic transition. This is achieved by locking the laser to the desired transition using saturated absorption spectroscopy (SAS). There are two SAS systems in the setup. One uses the secondary output of the extended cavity (SAS I, see 3.3).

This is used to check if the laser is close to resonance. The locking during the experiment is done by another SAS using output light of one of the fiber amplifiers, modulated by an AOM.

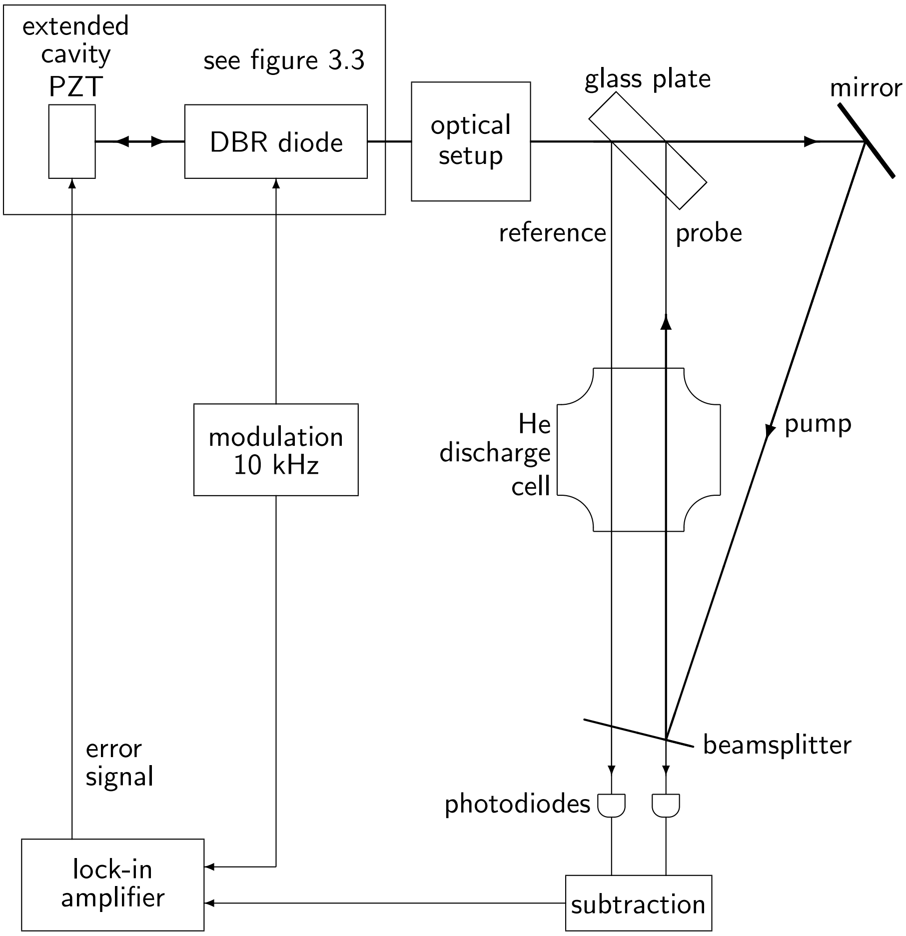

Figure 3.4 The frequency locking system uses part of the output of one fiber amplifier. The details of the optical setup are illustrated in figure 3.1, but note that this system follows any frequency drift of the diode. Therefore, the output of the laser is stabilized by applying the error signal derived by the lock-in amplifier to the PZT in the extended cavity (see figure 3.3).

A RF discharge in a He cell produces a plasma containing He* for spectroscopy. To make absorption lines visible on an oscilloscope, the laser frequency is modulated by ramping the extended cavity PZT. A single beam passing the cell would give a Doppler broadened absorption signal. To get sub-Doppler resolution, two relatively weak beams are used. One of these beams (probe) overlaps inside the cell with a strong counterpropagating beam (pump). When the laser is on resonance, all atoms that have a velocity component along these beams equal to zero are saturated by the pump and can not absorb the light of probe. Therefore, probe gives a Doppler broadened absorption signal with a sharp dip. The signal of probe and the other weak test beam (reference) are subtracted and the result is a Doppler-free absorption peak.

The cavity length is adjusted by hand so that the laser frequency is on the top of the desired peak, and then the locking system is activated. The laser diode current, and therefore the frequency of the laser is modulated with a small amplitude at 10 kHz. The SAS signal is put in a lock-in amplifier with the current modulation as reference. The lock-in amplifier gives an error signal which is applied to the PZT of the extended cavity to close the feedback loop.

For the lithography experiment, the laser needs to stay on resonance for several tens of minutes. Since the frequency locking turns out to be very sensitive to temperature changes in the lab, the voltage driving the extended cavity PZT needs to be adjusted by hand to compensate a slow drift of the error signal. This could also be achieved by a more sophisticated feedback system with integral amplification of the error signal, but this locking system has been designed for atomic beam collimation experiments, which do not need high stability over such long time.

3.3 Four Frequency Production

To collimate an atomic beam, the bichromatic force requires light at four different frequencies (see section 1.2.4) in two beams. These four frequencies are produced by a single, double-passed acousto optic modulator (AOM). This so-called 4-ω-AOM is illustrated in figure 3.5.

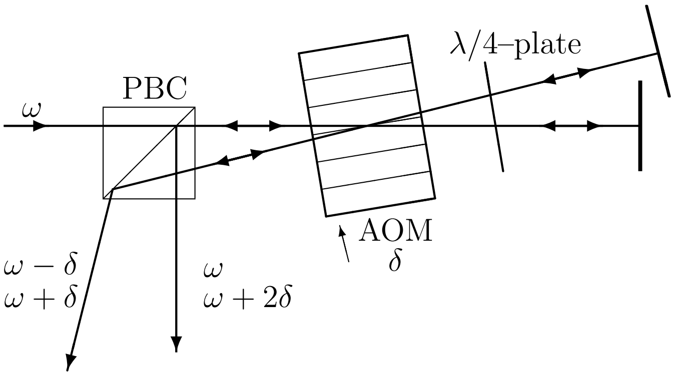

Figure 3.5 Production of four frequency light in two beams by a double-passed AOM. The $\lambda/4$ plate and the PBC separate the output spatially from the input. The arrow at the AOM indicates the direction of the sound wave.

The 0 and +1 diffraction orders are reflected back into the AOM, producing the two beams with four frequencies. The polarization direction is rotated by 90° using a double-passed $\frac{\lambda}{4}$–plate. This separates input and output beams spatially since the reflection inside the PBC is dependent on polarization.

The model for the bichromatic force (section 1.2.2) contains two frequencies of equal amplitude in each beam. The diffraction efficiency needs to be adjusted to get equal power into 0 and +1 diffraction order. This efficiency depends on the RF power driving the AOM and the angle of the incoming beam. The AOM is mounted on a six-axis motion stage to get the necessary fine control of the geometry. This is a very sensitive parameter and needs to be adjusted on a daily basis, whereas the RF power stays constant.

3.4 Amplification

Compared to optical molasses, bichromatic collimation requires high intensities. In addition, the beams need to have a certain size to guarantee sufficient interaction time between light and moving atoms ($v{\sim}1000\frac{m}{s}$). This makes power on the order of several hundred milliwatts in each beam necessary. We use two Keopsys KPS-BT2-YFA-NLS-1083-40-COL fiber amplifiers (FAs) to reach such high power. These instruments use a fiber doped with ytterbium (Yb), which serves as gain medium. It is pumped by laser diodes at a wavelength of 975 nm. The amplifiers have a first gain stage which gives 150/190 mW output, almost independent of input power. In further stages, the current of two extra laser diodes can be adjusted to increase the output power. With all diodes running on their upper current limit, the output of each amplifier is about 4 W. At high power and narrow laser linewidth, nonlinear effects may occur in the fiber. The amplifiers were tested with the experimental parameters and no nonlinear effects were found, even at the power limit [3].

In order to avoid such effects, the output fibers have a larger core (9.2 μm) and are limited to a length of 70 cm. Unlike other fibers in the experiment, they have not been polished and connected in the lab, but are purchased from Keyopsys, the manufacturer of the fiber amplifiers, which is able to produce more sophisticated fiber ends. ThorLabs fiber couplers are used at the output end of the fibers. The resulting beam had a Gaussian profile with a waist of 800 μm [2].

The polarization of the output light depends on the mechanical condition of the fiber, since the degree of birefringence in the fiber depends on physical stress. Therefore, the position of input and output fibers were secured. In addition, the fiber amplifiers contain a device which adjustably squeezes part of the fiber, allowing fine control of the polarization.

These controls make the output linearly polarized to a high degree. Nevertheless, a polarizing beam splitter cube (PBC) is used after each fiber amplifier. The main output of these PBCs goes to the collimation experiment, the secondary output is used to analyze the spectrum.

3.5 Preparing the Beams for Bichromatic Collimation

The beams out of the fiber amplifiers need to be modified for the collimation experiment. We adjust beam size, polarization and phase difference between the pulses of $+kv$ and $-kv$ beam.

3.5.1 Phase Matching

The direction of the bichromatic force depends on the relative phase of the two counterpropagating beams. This phase describes the relative timing of the excitation and deexcitation pulses in the π-pulse model. As mentioned in section 1.2.2, the optimal phase is $\frac{\pi}{2}$, if one pulse interval is 2π. The bichromatic detuning $\frac{\delta}{2\pi}$ in the experiment is 60 MHz, giving a spatial length of 1.25 m for one pulse. To match the phase of $+kv$ and $-kv$ beam, a variable delay path was inserted in the $+kv$ beam before the fiber amplifier. The relative phase of the two beams was measured by viewing the pulses in the beam with fast photodiodes (UDT InGaAs-100L) and a Tektronix 2445 oscilloscope [1]. The pathlength was roughly adjusted to match the relative phase close to $\frac{\pi}{2}$ [2]. The fine tuning was done with the delay stage while running the experiment and viewing the collimation on the phosphor screen.

3.5.2 Frequency Balancing

The model of the bichromatic force works with light of two frequencies whose amplitudes are of equal magnitude. To ensure that, we monitor the spectrum of the bichromatic beams with two Faby-Perot cavities using the small fraction output of the PBCs after the fiber amplifiers. The cavitylengths of these spectrum analyzers are scanned by PZTs and the transmitted light is detected by photodiodes. The output spectrum of each beam is displayed on an oscilloscope. The balancing of the amplitudes depends strongly on the alignment of the four-frequency AOM.

The Fabry-Perot cavities are also used to check the output of the fiber amplifiers for undesired effects like stimulated Brillouin scattering or stimulated Raman scattering. Both effects were observed in earlier experiments with polychromatic forces on metastable helium. These experiments used other FAs (which are now used e.g. for the molasses collimation stage) which were less reliable. Since these high power effects are suppressed by the design of the new amplifiers, they are not a problem in this experiment. A more detailed discussion can be found in [3].

3.5.3 Beam Expansion

The output of the fiber amplifiers is formed by single mode Gaussian beams with sub-mm waist. For collimation of an atomic beam, elliptical beam profiles are desired. Their long axis is oriented along the atomic beam, to provide sufficient interaction time between light and atoms. We use one spherical and one cylindrical telescope in each beam to shape the beam profiles. The spot size after these telescopes was measured by scanning a pinhole in front of a power meter perpendicular to the laser beam. The results are given in table 3.1:

	+ kv spot size/mm	**− kv** spot size/mm
vertical	5.4	5.6
horizontal	1.7	2.0

Table 3.1 Beam profiles of the bichromatic beams. We use the spot size definition given in [8].

It was found that the beams were slightly diverging ($\sim 10^{-4}$ rad), but, this leads only to a negligible intensity loss (compared to reflection/absorption on optical elements). The outer parts of the beam profile were cut by 10 mm diameter apertures. After that, the beams were split by 50/50 beamsplitters to provide each dimension with a $+kv$ and a $-kv$ beam.

Unlike optical molasses, each dimension of bichromatic collimation requires two interaction regions between light and atoms. In one of them, atoms with a positive velocity component along the laser beams are pushed to $v_\perp \sim 0$. The other interaction region does the same with atoms having a negative velocity component. Thus, the combination of two interaction regions provides collimation in one dimension. The experiment contains four interaction regions to achieve two-dimensional collimation. With a few mm separation between them the bichromatic collimation needs only an overall interaction length of 5 cm.

3.5.4 Beam Recycling

Each interaction region uses one $+kv$ and a counterpropagating $-kv$ beam. After passing one interaction region, each beam is reflected into the other interaction region of the same collimation dimension. This is called "beam recycling" since every incoming beam is used twice.

To assure the right value for the relative phase between two pulses, the optical pathlength of the beam recycling is important. This length needs to

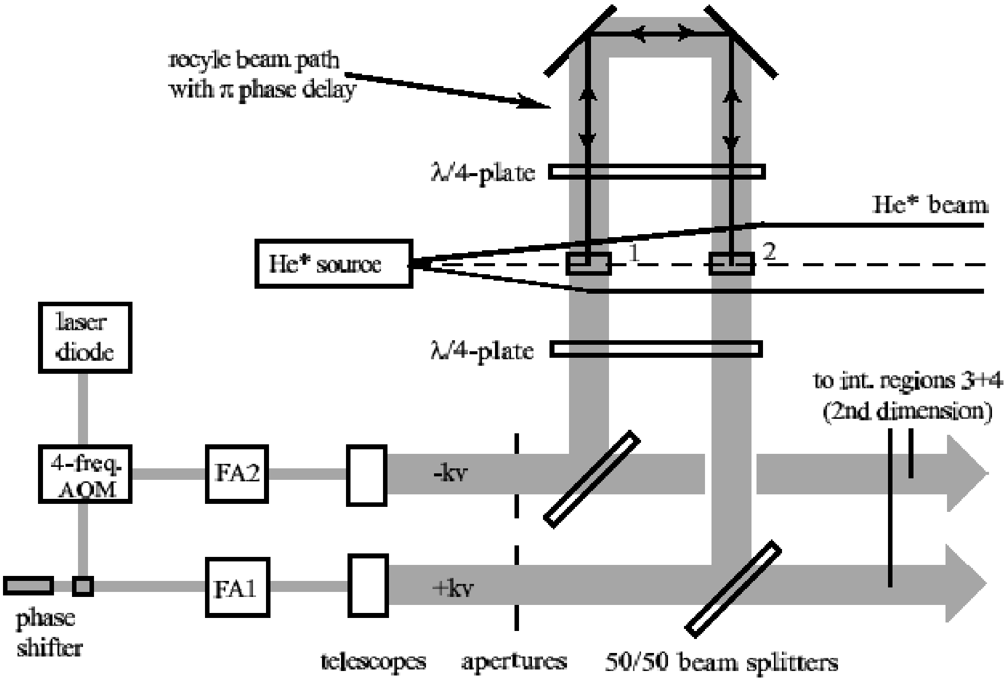

Figure 3.6 Diagram of the bichromatic beams after amplification. Each telescope in the picture contains a spherical and a cylindrical part, leading to elliptical beam profiles.

be an odd number times the length of one pulse (according to a phase of $(2n + 1)\pi$). In the experimental setup, this length is 125 cm, corresponding to a phase delay of π. Thus, the $+kv$ beam is ahead by $\frac{\pi}{2}$ in both interaction regions.

3.5.5 Polarization and Optical Pumping

Theoretical models describing the bichromatic force use the picture of a two-level atom. This is of course not the case for real atoms. If the light frequency in the experiment is close to an atomic transition, the respective levels dominate the behavior of the system and other levels can be neglected. In the experiment described here, optical frequencies are off-resonance by 60 MHz. The next closest transition (2^3S_1 to 2^3P_1) is more than 2 GHz higher than the $2^3\mathrm{S}_1$ to $2^3\mathrm{P}_2$ transition targeted in this experiment. Therefore, other levels give only negligible contributions to the behavior of the system.

However, both $2^3\mathrm{S}_1$ and $2^3\mathrm{P}_2$ consist of magnetic sublevels, which are degenerated in the case of no external fields. This atomic structure can not be neglected and needs further consideration. It is shown in figure 3.7.

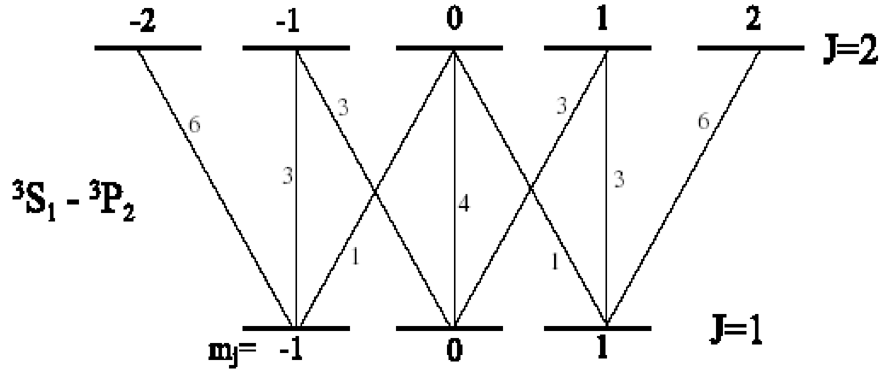

Figure 3.7 Sublevels of 2^3S_1 and 2^3P_2 with relative transition strengths. Transitions with $\Delta m_j = \pm 1$ are driven by $\sigma^{\pm}$–light.

In order to have only two relevant levels in the experiment, we use circularly polarized light. According to dipole selection rules, $\sigma^{\pm}$–light drives transitions with $\Delta m_j = \pm 1$. Spontaneous decay is not bound to this limitation and can have $\Delta m_j = \pm 1$ or 0. Thus, atoms are optically pumped into one of the cycling transitions $m_j = -1 \rightarrow -2$ or $m_j = 1 \rightarrow 2$. These levels form the effective two-level atom for the experiment.

Therefore, both beams need to have the same polarization (σ^+ or σ^-) in each interaction region. Since the two beams in each interaction region are counterpropagating, they need opposite helicity [5].

In the experiment, each beam passes a $\lambda/4$-plate directly before interacting with the atomic beam. The two plates for each interaction region are aligned to have their fast axis parallel so that their combination acts as a $\lambda/2$-plate, thus rotating linear polarization by 90°. The $+kv$ and $-kv$ beam are orthogonally linearly polarized before they enter the collimation setup. Due to the beam recycling method, the polarization of one of the beams is rotated by 90° before entering a certain interaction region (since it has to pass the other one with two $\lambda/4$-plates). The alignment of the waveplates in this interaction region assures that both beams are equally polarized (σ^+ or σ^-) while crossing the atomic beam.

3.6 Optical Molasses Stage

The bichromatic collimation provides a large capture range and a huge force. Nevertheless, the atoms still have a transverse velocity of $\sim 9\frac{m}{s}$ [3]. Compared to a traditional collimation by optical molasses, this velocity spread is significantly higher. To combine the advantages of both collimation methods in order to get a very bright beam, the bichromatic collimation was followed by an optical molasses collimation stage. This was suggested by a simulation shown in [3]. The measured beam parameters are presented in [2, 14]. The measurements on the quality of collimation show that the bichromatic stage collects a large number of atoms to a broad peak and optical molasses compresses this peak to get a strong increase in brightness.

In the experiment, an AOM is used to shift a part of the $-kv$ beam (see figure 3.1) by 82 MHz, giving two frequency components detuned by -8 MHz and 122 MHz. The latter one is too far from resonance and has no considerable effect on the atoms. The former gives a capture range according to the remaining velocity spread after bichromatic collimation. The light is injected into a third fiber amplifier to allow to use a wide intensity range. The gain of this amplifier is adjusted while running the experiment and measuring the quality for the collimation with the SSD.

This beam is not split to collimate separately in two dimensions, but passes the atomic beam once in each dimension and is then retroreflected. A $\frac{\lambda}{4}$-plate is used to adjust the polarization to be circular, but since the light is reflected several times after this waveplate, the polarization will hardly stay circular. It has been found experimentally that the quality of the collimation does not depend on the arrangement of this waveplate.

Chapter 4

Neutral Atom Lithography

In the first atomic nanofabrication experiments, structures were created directly by the particles that form the atomic beam (direct deposition). In neutral atom lithography (NAL), the exposure causes a local change of surface properties. This pattern is then transformed to permanent structures by etching the top layer of the sample. This chapter describes the chemical steps that are necessary to perform NAL before and after the exposure to the beam of metastable helium.

4.1 Samples

The substrate of the samples is formed by industry-standard silicon wafers. They have a diameter of 2" and are purchased from Wafer World Inc. One side is polished to provide a smooth surface. The other specifications can be

diameter	2” (50.8 mm)
grade	test
surface finish	1 side polished
growth method	Cz
dopant	boron (P)
orientation	$\langle 100 \rangle$
resistivity	1-20 Ω cm
thickness	250-300 μm

Table 4.1 Properties of the silicon wafers used as sample substrate.

found in table 4.1. For the purpose of NAL, these wafers are coated with titanium as adhesion promoter (few nm) and 30 nm of gold. The coating has been done by e-beam evaporation in the Physics Department at Stony Brook.

The wafers are split into smaller pieces ($\sim$1.5 cm) by applying pressure with the edge of a stainless steel piece. These pieces are individually cleaned and exposed.

The cleaning is a very important step. Any surface contamination at this time can prevent the formation of the resist layer and result in defects after the etching. The samples are first rinsed several times with acetone and ethanol until no visible residues could be found on the surface. In the next step, a mixture of sulfuric acid and hydrogen peroxide (35 %) (piranha solution) is used to remove organic residues. This solution is self-heating and has to be used immediately. The sulfuric acid carbonizes organic material on the surface and hydrogen peroxide oxidizes the remains to carbon dioxide. The mixture is highly corrosive and has to be treated with extreme care (heavy gloves, goggles) in a fume hood. The samples stay in this solution for 5-10 minutes. Afterwards, they are rinsed with pure ethanol several times to remove piranha residues.

4.2 Self-Assembled Monolayer (SAM)

The organic resist layer for the lithography process is formed by alkanethiols. These molecules consist of alkane chains with an alcohol-like head group (–S–H instead of –O–H). This part attaches to the gold layer on the sample in a chemical process described by:

$$\mathrm{R{-}SH} + \mathrm{Au}_n^0 \rightarrow \mathrm{RS^-{-}Au^+} + \frac{1}{2}\mathrm{H}_2 + \mathrm{Au}_{n-1}^0 \tag{4.1}$$

The energy of this bond is $\sim 200 \frac{kJ}{mol}$ [33] which makes it relatively stable. The alkanethiols form a self-organized lattice on the surface. The alkane-like tail groups make the surface hydrophobic and prevent further molecules from bonding to the gold layer. Therefore, this resist is called self-assembled monolayer (SAM).

The SAM in the experiment is formed by nonanethiol, purchased from Sigma-Aldrich (1-Nonanethiol, technical $\geq$95 %). After cleaning the samples with piranha solution and rinsing them with ethanol, we put them into a $1.5 \times 10^{-3} \frac{mol}{l}$ solution of nonanethiol in pure alcohol (200 Proof, ACS/USP grade, Pharmco Products Inc.) for 24 hours. For each sample, we use ∼80 ml of solution in an individual beaker. The amount of nonanethiol is determined by weight on a lab scale with accuracy of 2 mg. The solution is mixed directly before use.

After removing the samples from this solution, they are instantly mounted on a sample holder and put into the vacuum system. The SAM is very sensitive to physical and chemical threats, which makes several precautions necessary. For example, the loading chamber is roughed out and vented to atmospheric pressure very slowly ($\sim$1-2$\frac{torr}{s}$). In addition, no ion gauges are used when a sample is in the system. All pressure measurements are done in control runs without samples.

During the exposure, metastable helium atoms which hit the surface and release their energy. The ionization energy of the resist molecules is ∼10 eV, about half of the energy carried by metastable helium atoms. Dependent on their energy, released electrons can attack and ionize further resist molecules. The relevant scattering length of electrons in the SAM is < 1 nm [29], which leads to negligible structure broadening.

The ability to damage alkanethiol molecules depends strongly on the energy of the metastable state. The required dose for exposures using Ar* (12 eV) is ~15 times bigger than for those using He* (20 eV) [24].

4.3 Wet Etching

While being exposed to the beam of metastable helium, a mechanical mask (electron microscopy grid, 2000 Mesh, obtained from EMS) defines spots on the sample where He* can damage the resist. Where the SAM remains, the surface has hydrophobic character due to the unpolar tail group of the alkanethiol molecules. A water based etching solution attacks selectively parts of the gold layer which are not protected by the SAM while parts with an intact SAM are not affected. The whole exposure/etching process is shown schematically in figure 4.1.

The etching solution was developed by Xia et. al. [20] and has been used in several similar experiments [23, 24, 26]. In our experiments, we use 250 ml of this etching solution for each sample. The constituents are shown in table 4.2.

Potassium Thiosulfate (purum, ≥96%), Potassium Ferricyanide (99+%, ACS reagent) and Potassium Ferrocyanide (99%, ACS reagent) are purchased from Sigma-Aldrich, Potassium Hydroxide is obtained through the chemistry department at Stony Brook and manufactured by Fisher Scientific. The weight

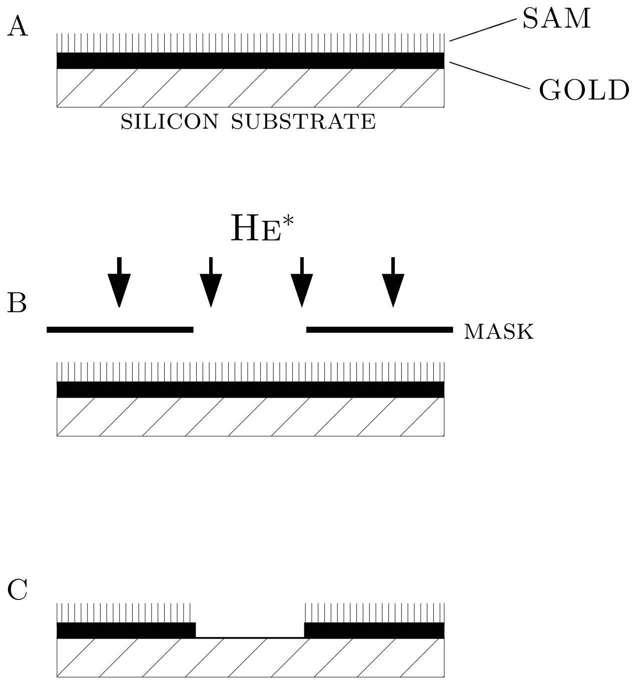

Figure 4.1 Sample during several steps of the lithography process. A: sample with self-assembled monolayer of an alkanethiol; B: exposure to He*; C: after etching, the structure of the mask is transferred to the gold layer. The adhesion layer is not shown.

is determined by a lab scale with accuracy of 2 mg.

During the etching process, the solution was stirred by a magnetic stirrer.

The gold is removed according to the electrochemical equations:

Chemical Name	Formula	c $[\frac{mol}{l}]$	Amount Used
Potassium Hydroxide	KOH	1	15.585 g
Potassium Thiosulfate	$K_2S_2O_3$	0.1	4.785 g
Potassium Ferricyanide (III)	$K_3Fe(CN)_6$	0.01	0.823 g
Potassium Ferrocyanide (II) Trihydrate	$K_4Fe(CN)_6 \cdot 3\ H_2O$	0.001	0.102 g
Distilled Water	H_2O	solvent	250 ml

Table 4.2 Chemicals used in the etching process. Note: Potassium Hydroxide is highly hygroscopic and naturally contains water. For the calculation of the used amount, 10 % water (by weight) are assumed.

$$\mathrm{Au^0} + 2\,\mathrm{S_2O_3^{2-}} \rightarrow \mathrm{Au(S_2O_3)_2^{3-}} + \mathrm{e^-} \tag{4.2}$$

$$\mathrm{Au^0} + 2\,\mathrm{OH^-} \rightarrow \mathrm{Au(OH)_2^-} + \mathrm{e^-} \tag{4.3}$$

$$\mathrm{Au(OH)_2^-} + 2\,\mathrm{S_2O_3^{2-}} \rightarrow \mathrm{Au(S_2O_3)_2^{3-}} + 2\,\mathrm{OH^-} \tag{4.4}$$

$$\mathrm{Fe(CN)_6^{3-}} + \mathrm{e^-} \rightarrow \mathrm{Fe(CN)_6^{4-}} \tag{4.5}$$

The ferrocyanide does not appear in this equations, but it reduces defects in the SAM covered parts of the gold layer [20]. The etching solution is mixed directly before use. It shows aging effects (color change from bright to pale yellow) on the timescale of a few hours, which gives doubts about its effectivity after storage.

The etching time has been determined experimentally to be about 7 minutes.

If no SAM is formed or it is destroyed manually (e.g. at the edge of the sample by the holder), it takes only 4 min to remove the gold layer. This is consistent with the studies of Yamauchi et. al. [21], which showed that only a small part (CH_x^+ or H^+) of the alkanethiol molecule is removed by He^* impact. This shortens the polar tail, resulting in reduced hydrophobicity.

During the whole lithography process, the samples stay under vacuum for 25 min plus exposure time (pumpdown, venting, alignment). The time from removing the samples from the SAM solution to the etching is about 45 min plus exposure time.

After being etched, the samples are cleaned with distilled water and glued on microscope slides. The analysis of the structures is done using an atomic force microscope (AFM).

Chapter 5

Results

5.1 He* Flux Measurement

The detectors in the beamline allow the measurement of several beam parameters. For the work presented here, the beam intensity has been measured near the sample in order to determine exposure doses. With the current detectors, we can also measure beam divergence, which is very important for NAL using an optical light mask. The measurement of these beam parameters is also used to assure proper function of the source and to check the alignment of the collimation beams, before lithography samples are exposed.

5.1.1 MCP/Phosphor Screen

The MCP/phosphor screen detector gives a coarse, but fast image of the atomic beam. The camera system can run in real-time video mode and also take pictures. These are saved and analyzed as bitmap (.bmp) files. The MCP is 22 cm away from the skimmer and has a diameter of 25 mm. This gives a range of detection angles of 110 mrad or $\pm 57\frac{m}{s}$ transverse velocity. On the images, the diameter of the MCP is roughly 300 pixels.

During the alignment process, the phosphor screen is used to check the efficiency of the individual stages. Figure 5.1 shows the pictures of each stage. The bichromatic collimation is very effective in the first dimension (picture A), because the interaction regions are close to the skimmer. Picture B shows full bichromatic collimation. The "wings" of the second dimension are only slightly visible, showing the reduced efficiency in comparison to the first dimension. Compared to optical molasses, the atomic beam spot size is larger. This shows that while the bichromatic force does not collimate to very low transverse velocities, it shows a large capture range, which exceeds the phosphor screen. This can be seen in the outer parts of picture B, which are darker than those of picture C (molasses collimation). Picture D shows the combination of both methods. The bright spot indicates a high peak intensity. At this spot, the imaging system saturates. The resulting atomic beam profile is not isotropic,

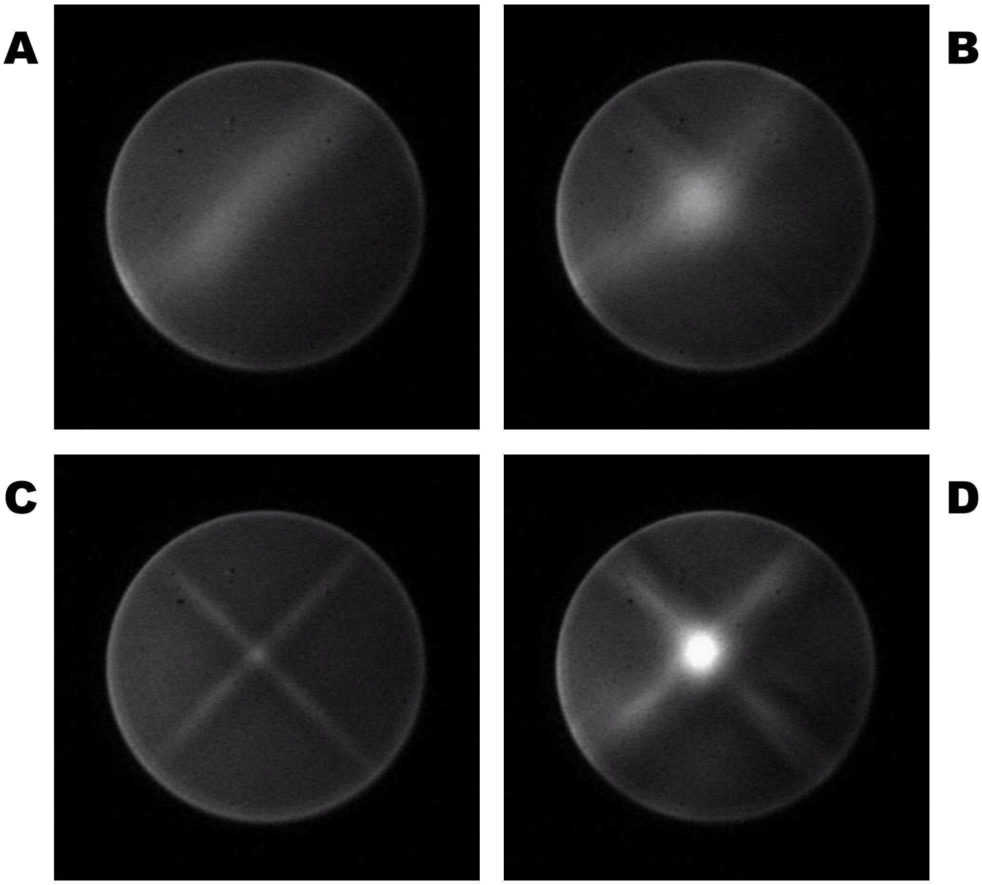

Figure 5.1 Different collimation methods viewed by the MCP/phosphor screen detector. A: bichromatic collimation in one dimension, B: bichromatic collimation in both dimensions, C: molasses collimation, D: combined bichromatic/molasses collimation. For these pictures, -500 V have been applied to the MCP and 1400 V to the phosphor screen.

but shows clearly the single collimation dimensions in the outer parts of the screen. The settings (voltage applied to MCP and phosphor screen) for all four pictures are the same.

The MCP/phosphor screen gives a qualitative picture of the atomic beam. Any large discrepancy from ideal collimation parameters can be detected quickly and easily. This detector also shows off-center parts of the atomic beam, which are only accessible to a limited extend by the SSD. These features makes this detector invaluable for both individual and mutual alignment of the collimation stages.

5.1.2 SSD Measurements

The detected SSD signal is the current between back plate and ground (see figure 2.5). This current ranges from ∼5 to ∼60 pA. This current is not only due to metastable helium, but there are also contributions from UV light and charged particles. The latter contribution is presumed to be very small, since we have several deflection fields (electric and magnetic) in the system. This assumption is supported by the fact that the observed signal does not show the strong fluctuations we detect without deflection fields. The ultraviolet contribution has been determined in a blue molasses experiment. This uses the scheme of optical molasses collimation, but with a blue detuned laser. This reverses the sign of the force (see equation 1.9) and removes metastable atoms out of the center of the beam. A SSD in the center is used to determine the contribution due to metastables and UV. It is assumed that their ratio stays constant over the scan range. If there is a contribution from charged particles in the signal despite the presence of deflection fields, it will be unaffected by the blue molasses beams and subtracted as UV signal. This works well in the center of the atomic beam and therefore in the relevant area for our neutral atom lithography experiments. Nevertheless, inhomogenities in this contribution due to electromagnetic fields can affect the measured beam profile in the off-center parts.

The blue molasses uses the molasses collimation stage of the beamline. The respective AOM was set to 94 MHz (instead of 82 MHz, giving a detuning $\delta = 2\pi{\cdot}4$ MHz=2.5 γ. The bichromatic collimation beams are blocked. The intensity is adjusted by the gain of the molasses FA to minimize SSD current in the center. The measured UV contribution is subtracted off the detected currents.

We also observed constant, finite current signals with the atomic beam blocked by the MCP/phosphor screen. The raw signal is modified by this offset and the UV part. This gives the SSD current I_{SSD,He^*} which is caused by the impact of He* atoms. The atomic flux is calculated by this modified current, the geometry of the detector and the efficiency for electron extraction (70 %, [16]). The width of the slits is determined by diffraction of a He-Ne laser to 0.278 mm (front) and 0.5 mm (back):

$$I_{\mathrm{He}^*} = \frac{I_{SSD,He^*}}{0.7 \cdot e \cdot 0.278\mathrm{mm} \cdot 0.5\mathrm{mm}} \tag{5.1}$$

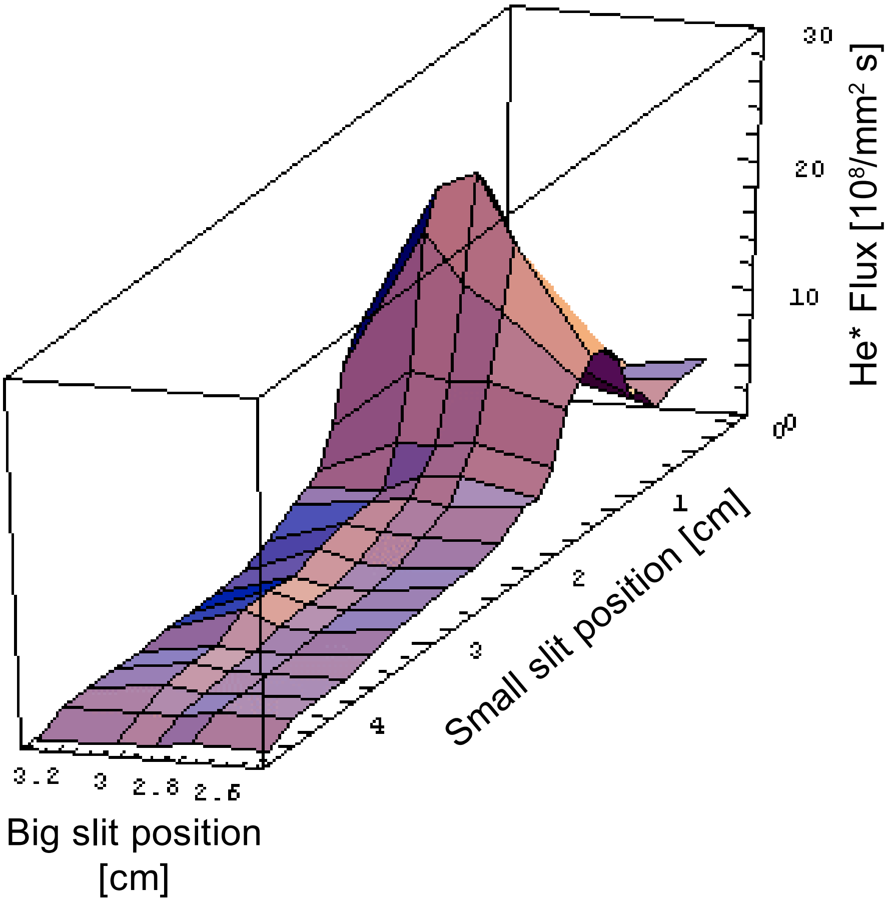

Figure 5.2 Surface plot of the atomic beam cross section (full collimation). The asymmetry in the plot is due to the different scan ranges in the two dimensions.

Scans of the atomic beam cross section have been done with the crossed slit SSD 56 cm away from the skimmer (at this time, the gate valve was not part of the system and therefore the beamline was shorter). Figure 5.2 is a surface plot of the fully collimated atomic beam. The peak flux is $28 \cdot 10^8 \frac{1}{mm^2 \cdot s}$. The FWHM is 6 mm. Figure 5.3 shows a scan of the small slit with the big slit fixed

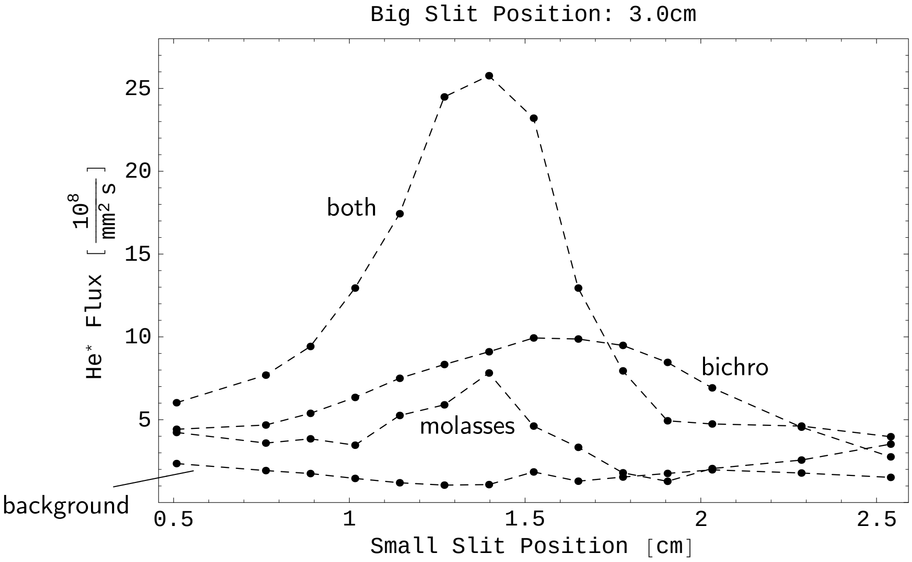

Figure 5.3 Metastable helium beam flux profile. This plot represents a part of figure 5.2 with the big slit fixed at 3.0 cm. The four set of points represent background (no collimation), molasses and bichromatic acting alone and combined collimation (both). Curves are drawn to guide the eye.

at 3.0 cm. The four curves represent background (all beams blocked), bichromatic collimation (molasses beam blocked), molasses collimation (bichromatic beams blocked) and combined collimation (no beams blocked). It is clearly visible, that the position of the combined peak is determined by the molasses stage. The molasses capture range is smaller than the range of these scans, but due to the scan direction along the "wings" (upper left to lower right on the pictures in figure 5.1), the flux for molasses is almost uniformly higher than the background. Respective plots for other positions of the big slit are given in appendix A. For these scans, the source was running at a discharge current of 6 mA at a helium outlet pressure of 1.2 torr.

These detected data showed good repeatability in several runs of the experiment. However, the accuracy of the results is limited by systematic effects. The detected current depends on the SSD front plate voltage as well as on the voltage applied to the deflection plates. The typical parameter set was found to give conclusive data [3], but it also shows the precision limitation. Another indication for systematic effects is the comparison between different detector designs. For earlier He^* collimation work, the back SSD had a different design, which allowed only 1D scans. Even without changing the physical parameters, our current SSD shows lower signals than the difference in aperture size indicates. These effects lead to an estimate of a systematic error of 30 %.

The plots cover a transverse velocity range of $\pm 20\frac{m}{s}$. Due to inhomogeneous intensity in the bichromatic beams, the experimental capture range is even larger ($\pm 87\frac{m}{s}$, [2]) than indicated by the force profile (figure 1.5). This gives the large increase of the total number of atoms in the scan range, which can be seen in figure 5.3. The additional collimation with optical molasses gives a narrower peak, increasing the flux by a factor of more than 2.5. This is higher than the sum of both collimation stages acting on their own, showing the efficiency of this method. The width of this peak leads to an estimate of

$5.5\frac{m}{s}$ for the remaining transverse velocity. This is almost one order of magnitude higher than the Doppler limit, which can be explained with the short interaction time of 20 ms and the high molasses detuning of 5γ.

The collimation with the bichromatic force was found to be less effective than expected because only 1/3 of the source output is collected in the central peak. The main reason for that is finite optical pumping time. The metastable ground state (2^3S_1) is formed by three sublevels (see figure 3.7). Only for one of them, the conditions of a two-level atom are met and therefore only part of the atoms are subject to the full bichromatic force. If an atom starts out in another ground state sublevel, it is optically pumped to the desired transition. This takes place in the bichromatic interaction regions and needs roughly as long as the interaction time with the laser beams. Therefore, atoms which are not in the right ground state level in the beginning are not collimated effectively. It is planned to add an optical pumping stage to get all the atoms to the right sublevel before collimation, which should increase the efficiency of the bichromatic collimation.

5.2 Lithography

5.2.1 Atomic Force Microscope (AFM)

We analyze the structures we created with an atomic force microscope (AFM), model Q-Scope^{TM} 350 from Quesant. This scanning probe instrument measures a microscopic, two-dimensional height profile of the sample with high resolution (sub nm). The software running the AFM produces pseudocolor images of the surface structure. The raw data can also be extracted by a separate program, which puts out text files, that be further analyzed with any data processing software.

The sensitive part of the AFM is a sharp, 15-20 μm long silicon tip on a cantilever (several hundred μm long) of the same material. When the tip is close to the surface of the sample, the force between tip and surface bends the cantilever. To detect this movement, a laser is reflected from its back side and registered by a photodetector. A PZT tube controls both the height of the tip above the surface and the lateral position.

We operate the AFM in intermittent-contact mode. In this mode, the cantilever is set to oscillation near its resonance frequency ($\sim$170 kHz) with an amplitude of typically 100 nm. If one of the turning points is close to the surface, this vibration is damped. The vertical position of the tip is adjusted by the PZT tube until the damping reaches a preset value (typically ∼15 %). While scanning across the surface, a PID feedback loop keeps this damping constant by moving the probe vertically. The relative height on the surface is measured as the voltage applied to the vertical movement PZT.

The AFM in the lab offers a feature called "broadband mode", which can be used to improve quality and speed of the scans. In this mode, the error signal (measured damping – preset damping) which feeds the electronics to control the PZT is calibrated and added to the measured height value. Therefore, a finite error signal is tolerable, which allows higher scanning speed without reducing the accuracy. This method is limited by nonlinearity in the calibration of the error signal.

5.2.2 Results

The samples which are analyzed by the AFM are usually slightly tilted. For the maximum scan size of 40 μm, this tilt is ∼1 μm and therefore much larger than the height of created structures (30 nm). The AFM software offers several methods to remove the tilt, but all of these can create artifacts in the resulting data. The mode that was usually used fits each horizontal line with a polynomial of second order and subtracts this fit ("parabolic line by line").

The quality of the created structures depends strongly on exposure dose

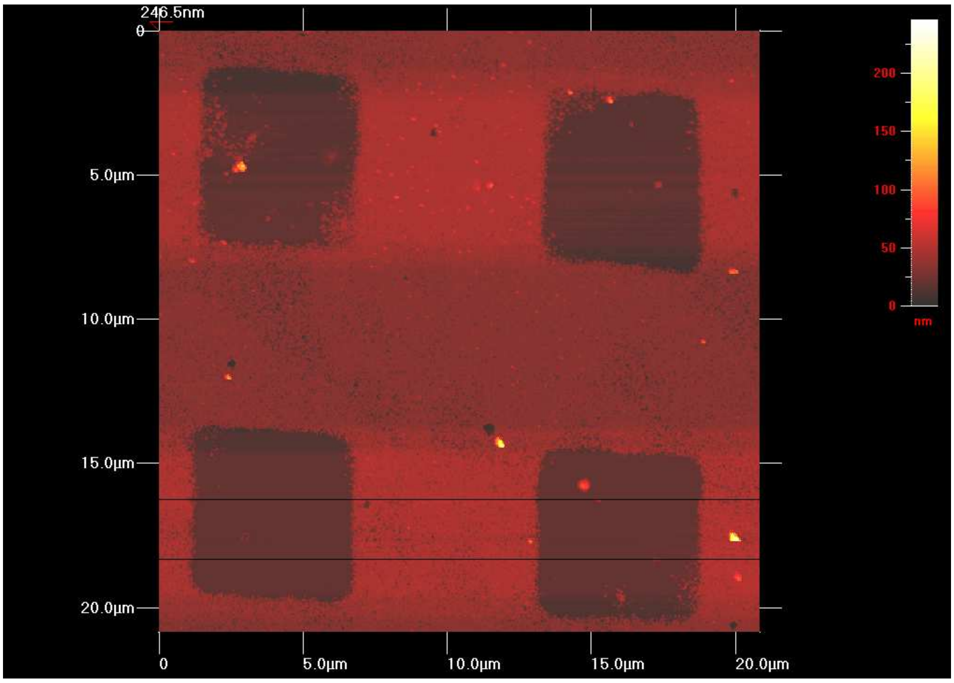

Figure 5.4 Pseudocolor image produces by the AFM software. The brightness indicates the height of each pixel. This sample shows "good" exposure and has been etched for the right time, which makes the squares defined by the mask clearly visible. Several bright spots on the surface indicate contamination. The relative dark part in the vertical center is an artifact of the tilt removal, which treats each horizontal line separately (see text). The are between the black lines is averaged horizontally and presented as lineout in figure 5.6.

and etching time. The sample in figure 5.4 shows good visible structures (dark squares), indicating sufficient exposure ($5.6 \times 10^{12} \frac{He^{*}\ atoms}{mm^2}$) and the right etching time (7 minutes). The parts where the gold is etched away are clearly visible and correspond to the open parts of the mask (micromesh). Besides these squares, there are several dark spots indicating removal of gold. These spots have about the same size as contaminations on the surface (bright spots) which makes such contaminations in earlier lithography steps a possible reason, why no SAM has been formed there, leaving the surface unprotected during etching.

The exposure dose is determined by the peak flux of the atomic beam, which is measured before the actual experiment (see section 5.1.2 for details), and the exposure time (typically 20-40 min). The minimum dose to get features without gold grains in the etched parts was found to be $2.8 \times 10^{12} \frac{He^*\ atoms}{mm^2}$. With higher doses, the individual features do not change noticeable, but the area where they can be found on the sample increases. For $5.6 \times 10^{12} \frac{He^*\ atoms}{mm^2}$ it was larger than the AFM stage movement range (1 cm × 1 cm). Figure 5.4 shows a part of this sample. A systematic function between exposure dose and this spot size could not be found since the quality of the features decreases continuously in the off-center parts and hard criteria for a quantitative analysis could not be defined and/or measured. In addition, the aperture of the sample holder limits the area, where features can be created. However, qualitative comparisons between different samples showed a noticeable increase of the spot size with the exposure dose.

Figure 5.5 shows a sample which was exposed to $2.0 \times 10^{12} \frac{He^*\ atoms}{mm^2}$. The square, where the gold is supposed to be etched away is noticeable, but depth and roughness indicate remaining gold there. This is supported by the pre-

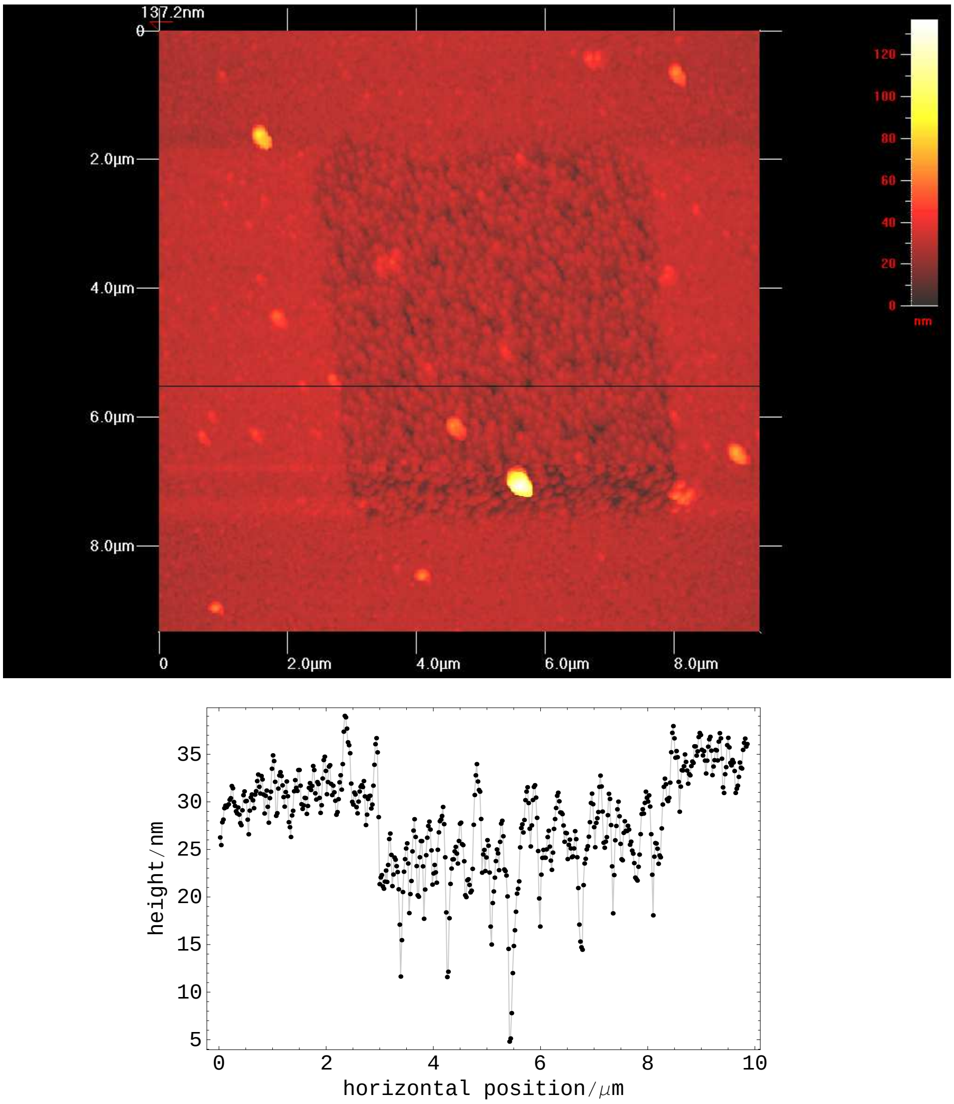

Figure 5.5 Pseudocolor image of underexposed sample and height profile along black line. The height profile shows the position of the feature visible in the picture, but due to underexposure, the gold is not completely etched. The curve in the plot is drawn to guide the eye.

sented height profile. Inside the square, the average height is lower and the roughness is strongly increased. Certain spots are etched down to the silicon substrate. Such features can not only be found on underexposed samples, but also in the outer parts of such exposed to higher doses. That supports the assumption of underexposure for this effect, even though under-etched samples show similar properties.

The sufficient dose to damage the SAM is close to the number found in similar experiments [26], but, according to [33], we assumed 0.21 nm^2 for the effective area of one alkanethiol molecule on the surface (instead of 0.1 nm^2 in [26, 29]). This gives an exposure dose of 0.59 He* atoms per resist molecule, which supports the theory that the SAM not only gets damaged by He* atoms itself, but also by released electrons. The internal energy of metastable helium is about twice the ionization energy of an alkanethiol molecule and therefore released electrons might cause further ionization.

Figure 5.6 presents a height profile of the sample shown in figure 5.4. Each point is averaged over 51 lines (vertically), as indicated by the black lines in figure 5.4. The height of the features is $\sim$25 nm, close to the thickness of the gold layer (30 nm). In addition, the roughness of the lower parts is clearly less than in the upper ones, indicating that the gold is etched completely and the AFM detects the substrate. This difference is even more visible in lineouts of single pixel lines.

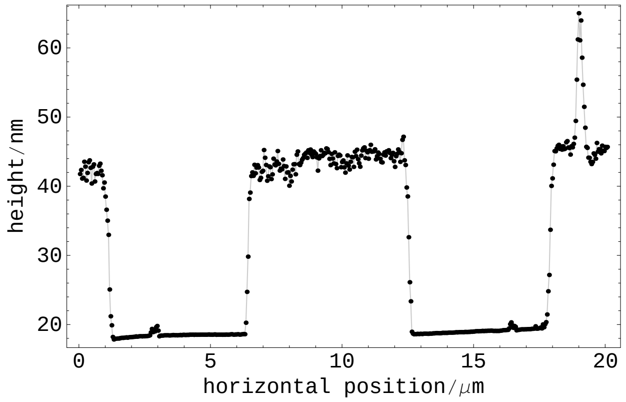

Figure 5.6 Horizontal lineout of the AFM scan shown in figure 5.4. Each point shows the average over a vertical section (51 pixels) indicated by the black lines in the image above. The spike on the right is due to contamination on the surface. The curve is drawn to guide the eye.

From figure 5.6, the width of the etched part is determined to be 5.2 μm and the periodicity of the structures to be 11.3 μm. The uncertainty of this measurement is mainly due to creep in the PZT elements of the AFM. These do not only respond (as supposed) on very short timescales, but show a small drift over several minutes. The AFM in the lab measures the movement of the PZTs by the applied voltage and does not take such long time effects into account, which leads to a relative error of 20 % in AFM measurements. More sophisticated instruments measure the PZT movement separately by capacitive sensors.

The electron microscopy grid consists of 2000 wires per inch (2000 Mesh, manufacturer's specifications) and is therefore supposed to give a periodicity of 12.5 μm. The difference between this and the measured value is within the tolerance of the AFM.

5.2.3 Resolution

The edges of the created structures are of special interest because their analysis gives information about the resolution of this lithography method. Here, the resolution is defined as the lateral width, where the feature height rises from 10 % to 90 % of its total value. For this analysis, a part of a 40 micron picture was selected and scanned again (hard zoom). The size of these scans is about 5 μm and they contain 1000×1000 data points, giving a lateral resolution of $\sim$5 nm, about one order of magnitude smaller than the expected edge resolution [29, 30].

Figure 5.7 shows one of these detail scans. On the right side (dark color), the etching solution removed the gold from the surface. The border between the low (dark) and high (bright) part is not a straight line, but shows some structure. This is be due to the graininess of the gold, which is also observable on the left side. The resolution was determined using a Mathematica code. This code first removes the tilt, because the default method does not work well if the structures are about the scan size or bigger. The analysis of single,

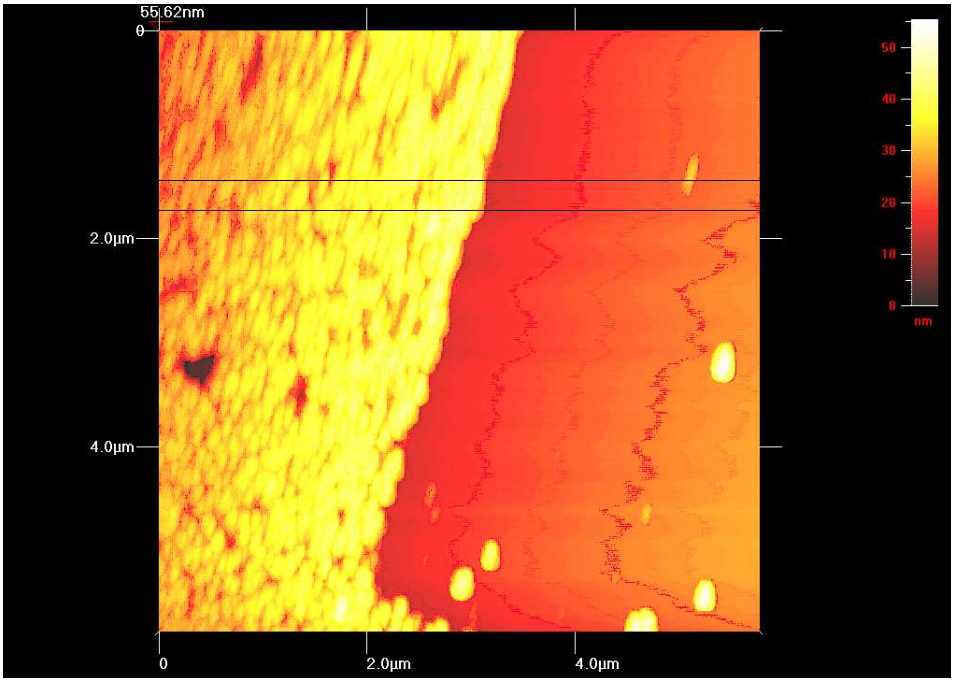

Figure 5.7 Detail scan to analyze edge resolution. The scan contains 1000×1000 data points (resolution ∼5 nm). The edge is analyzed by averaging pixel values between the black lines.

horizontal lines showed strongly varying resolution values. Therefore, we took the average over 51 horizontal lines. To take the angle between scanning direction and feature edge into account, each line was shifted horizontally by a "direction" parameter. The obtained resolution is the minimum as a function of this parameter. The horizontal lines indicate the averaging interval.

The evaluation of the edge shown in figure 5.7 is given in figure 5.8. The horizontal lines show 10 % and 90 % of the step height. This sample was exposed to $2.8 \times 10^{12} \frac{He^{*}\ atoms}{mm^{2}}$ and gave best results for the resolution which

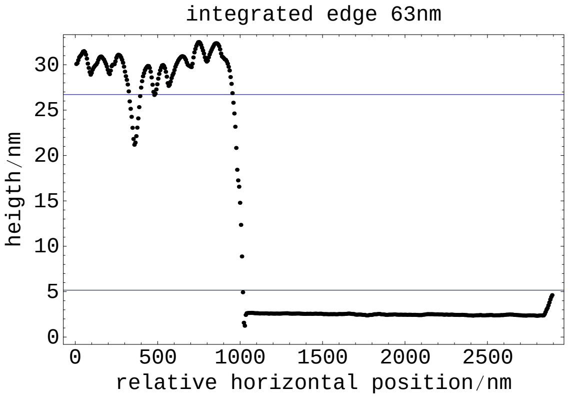

Figure 5.8 Edge resolution of the scan shown in figure 5.7. The average interval is given by the two black lines in 5.7 and a “direction” parameter is used in the averaging process (details see text). The horizontal lines indicate the 10 % and 90 % height of the edge, which are used to define the resolution.

is determined to be 63 nm. Individual lines showed values down to ∼30 nm, which corresponds to the thickness of the gold layer and is about the expected limit. Exposure to double the dose gave resolution values on the order of 140 nm, but the small number of high quality exposures up to now does not give clear results on a dependence to exposure doses. Also, we could not find clear dependence of the resolution on the position on the sample, which also corresponds to varying exposure dose.

The accuracy of the resolution analysis is affected by the error of the AFM. In addition, the edge is only about 10 pixels wide and the value depends on the position of the averaging interval. Therefore, the error is estimated to 25 %.

The mask does not affect the analysis presented here, but it might be important for the actual resolution value we measure. Besides the graininess of the gold layer, an imperfect mesh might cause the edge to become uneven. We can not measure the quality of the mesh and estimate its influence on the resolution. The planned experiments with a mask formed by an optical standing wave are supposed to bring more clarity to this case.

Resolution Limits Atom lithography does not suffer from diffraction limitation since the de-Broglie wavelength of the used atomic beams is smaller than the size of an atom. However, the resolution in our and comparable experiments is limited to several tens of nanometers. The measured values are not far away from the thickness of the gold layer. This might be an experimental limit since wet etching is an isotropic process, which does not allow an aspect ratio (step height/width) larger than one. On the other hand, the thickness of the gold layer can not be reduced arbitrarily, since this might lead to a more uneven and rough surface. Figure 5.8 shows grains of gold and that the surface is not a smooth gold layer in the unetched part. This can also be seen in fresh samples, that were not cleaned, exposed or etched. The solution to that might be secondary treatment of the gold layer (annealing) or different substrates, which support more uniform gold layers (e.g. mica, [32]).

Another limitation lies in the formation of the SAM. The case of a nonanethiol layer on a sputtered gold surface, which is exactly the same as in our experiment, has been studied by O'Dwyer et al. [33]. It was found, that the SAM is not a perfect lattice, but is formed by separated domains and contains several types of defects in high density. This leads the authors to estimate a resolution limit of ∼20 nm due to the SAM.

Chapter 6

Conclusion

The work presented here shows neutral atom lithography with metastable helium. Our setup exploits a unique collimation method using bichromatic light. The combination of this method and traditional optical molasses gives a high intensity beam, higher than the sum of each collimation method acting alone. We achieved a peak flux of $28 \cdot 10^8 \frac{1}{mm^2 \cdot s}$ at a position 56 cm away from the skimmer. Metastable helium is very useful for both bichromatic collimation and neutral atom lithography. The atomic transition at 1083 nm is accessible by diode lasers and the required high saturation parameter is, due to the low saturation intensity, available with moderate laser power. In addition, He*provides an internal energy of 20 eV, which is the highest value for metastable noble gas atoms. This energy enables the atoms to damage a hydrophobic, monomolecular resist layer of alkanethiols on gold coated lithography samples with high efficiency. The resolution of this method is 63 nm with a gold layer of 30 nm. We reach this resolution with an exposure dose of $2.8 \times 10^{12} \frac{He^{*}\ atoms}{mm^2}$ which corresponds to 0.59 He* atoms per resist molecule.

Exposure Time We need 20 minutes exposure time to reach this dose in our setup, but several improvements may reduce that in the near future. A planned optical pumping stage is supposed to increase the effectivity of the bichromatic collimation, that captures now only 1/3 of the source's output. In addition, an optical light mask serves as a microlens array to focus the atomic beam microscopically, increasing the atomic flux locally. With these improvements, the exposure time is expected to be decreased to 1 minute or less soon.

Bibliography

[1] M. Cashen

Ph.D. dissertation, SUNY Stony Brook, 2002

[2] M. Partlow

Ph.D. dissertation, SUNY Stony Brook, 2004

[3] J. Bochmann

Master thesis, SUNY Stony Brook, 2004

[4] T. Chuang

Ph.D. dissertation , SUNY Stony Brook, 1991

[5] M. Williams

Ph.D. dissertation , SUNY Stony Brook, 1999

[6] S. Petra

Ph.D. dissertation, Vrije Universiteit, 2004

[7] H. Metcalf, P. van der Straaten: *Laser Cooling and Trapping*, Springer, New York (2002)

[8] P. W. Milonni, J. H. Eberly: *Lasers*, John Wiley & Sons, New York (1988)

[9] A. Einstein
Physik. Zeit. **18**, 121 (1917)

[10] D. J. Wineland, W. M. Itano
Phys. Rev. A **20**, 1521 (1979)

[11] E. Kyröla and S. Stenholm
Opt. Commun. **22**, 123 (1977)

[12] M. Cashen and H. Metcalf
Phys. Rev. A **63**, 025406 (2001)

[13] M. Cashen and H. Metcalf
J. Opt. Soc. Am. B **20**, 915 (2003)

[14] M. Partlow, X. Miao, J. Bochmann, M. Cashen, and H. Metcalf
Phys. Rev. Lett. **93**, 213004 (2004)

[15] G. Woestenenk, J. Thomsen, M. van Rijnbach, P. van der Straten, and A. Niehaus
Rev. Sci. Instrum. **72**, 3842 (2001)

[16] F. B. Dunning, R. D. Rundel, and R. F. Stebbings
Rev. Sci. Instrum. **46**, 697 (1975)

[17] R. Grimm, J. Söding, and Y. Ovchinnikov
Opt. Lett. **19**, 658 (1994)

[18] W. Phillips and H. Metcalf
Phys. Rev. Lett. **48**, 596 (1982)

[19] J. Kawanaka, M. Hagiuda, K. Shimizu, and H. Takuma
Appl. Phys. B. **56**, 21 (1993)

[20] Y. Xia, X. Zhao, E. Kim and G. M. Whitesides
Chem. Mater. **7**, 2332 (1995)

[21] Y. Yamauchi, T. Suzuki, M. Kurahashi, and X. Ju
J. Phys. Chem. B **107**, 4107 (2003)

[22] D. Meschede and H. Metcalf
J. Phys. D: Appl. Phys. **36**, R17 (2003)

[23] K. K. Berggren, A. Bard, J. L. Wilbur, J. D. Gillaspy, A. G. Helg, J. J. McClelland, S. L. Rolston, W. D. Phillips, M. Prentiss, G. M. Whitesides
Science **269**, 1255 (1995)

[24] A. Bard, K. K. Berggren, J. L. Wilbur, J. D. Gillaspy, S. L. Rolston, J. J. McClelland, W. D. Phillips, M. Prentiss and G. M. Whitesides
J. Vac. Sci. Technol. B **15**, 1805 (1997)

[25] W. Lu, K. G. H. Baldwin, M. D. Hoogerland, S. J. Buckman, T. J. Senden, T. E. Sheridan, and R. W. Boswell
J. Vac. Sci. Technol. B **16**, 3846 (1998)

[26] B. Brezger, T. Schulze, U. Drodofsky, J. Stuhler, S. Nowak, T. Pfau, and J. Mlynek
J. Vac. Sci. Technol. B **15**, 2905 (1997)

[27] M. Kreis, F. Lison, D. Haubrich, D. Meschede, S. Nowak, T. Pfau, J. Mlynek
Appl. Phys. B **63**, 649 (1996)

[28] K. S. Johnson, K. K. Berggren, A. Black, C. T. Black, A. P. Chu, N. H. Dekker, D. C. Ralph, J. H. Thywissen, R. Younkin, M. Tinkham, M. Prentiss, and G. M. Whitesides
Appl. Phys. Lett. **69**, 2773 (1996)

[29] A. S. Bell, T. Pfau, U. Drodofsky, J. Stuhler, T. Schulze, B. Brezger, S. Nowak, and J. Mlynek
Microelectron. Eng. **41/42**, 587 (1998)

[30] S. J. H. Petra, L. Feenstra, W. Hogervorst, W. Vaasen
Appl. Phys. B. **78**, 133 (2003)

[31] X. Ju, M. Kurahashi, T. Suzuki and Y. Yamauchi
Jpn. J. Appl. Phys. **42**, 4767 (2003)

[32] X. Ju, M. Kurahashi, T. Suzuki, and Y. Yamauchi
J. Vac. Sci. Technol. B. **21**, 2478 (2003)

[33] C. O'Dwyer, G. Gay, B. Viaris de Lesegno, and J. Weiner
Langmuir **20**, 8172 (2004)

Appendix A

Atomic Beam Profile

In this appendix, a full set of lineouts across the atomic beam is presented. These lineouts are similar to figure 5.3 (page 77), with the big slit in fixed position. The curves are drawn to guide the eye.

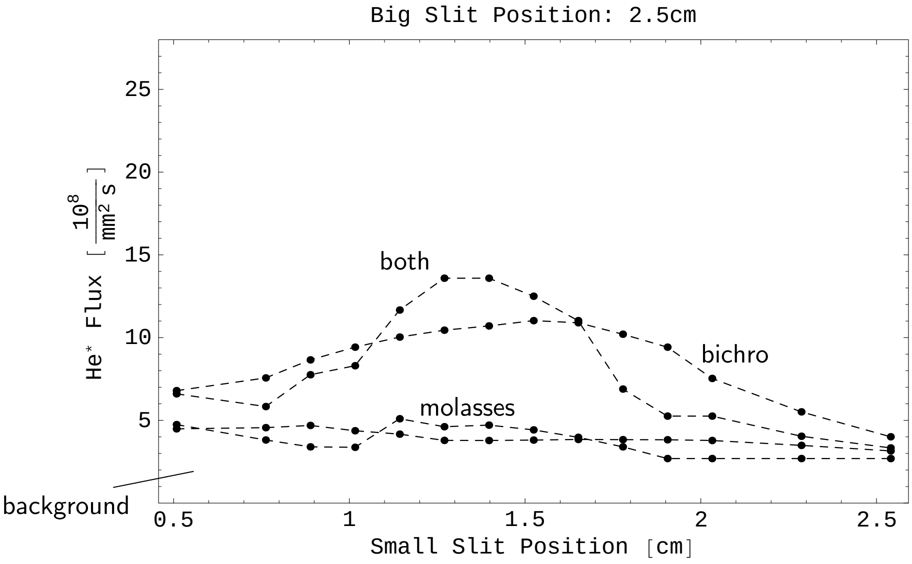

Figure A.1 Atomic beam cross section with the big slit of the SSD at 2.5 cm.

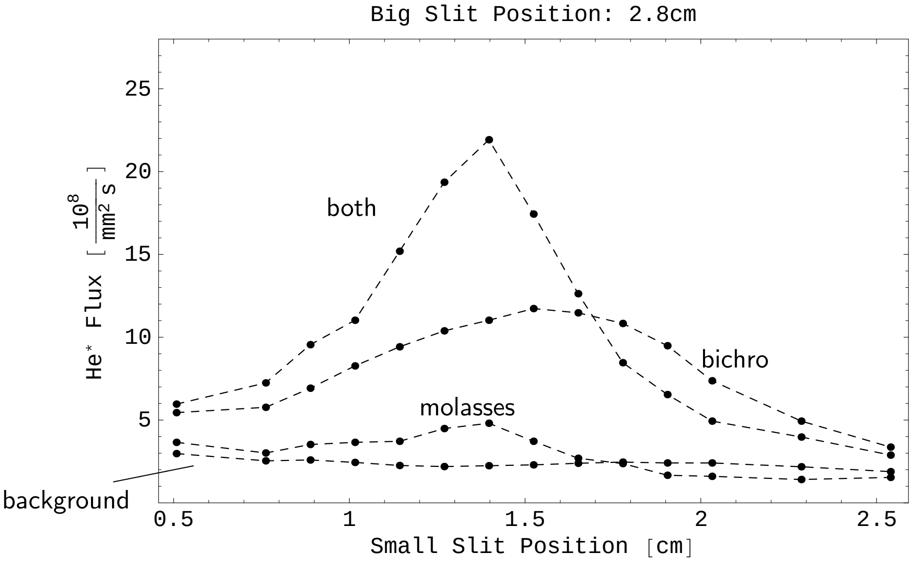

Figure A.2 Atomic beam cross section with the big slit of the SSD at 2.8 cm.

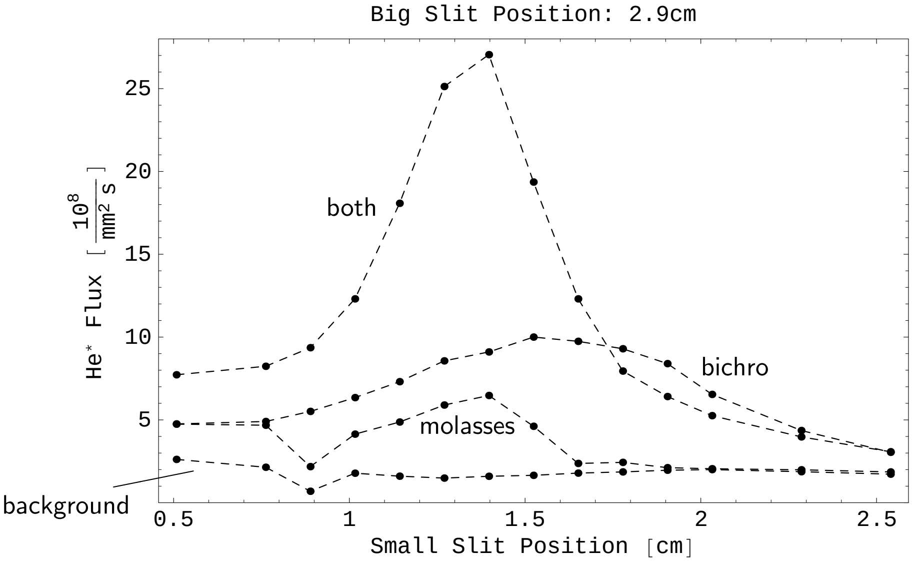

Figure A.3 Atomic beam cross section with the big slit of the SSD at 2.9 cm.

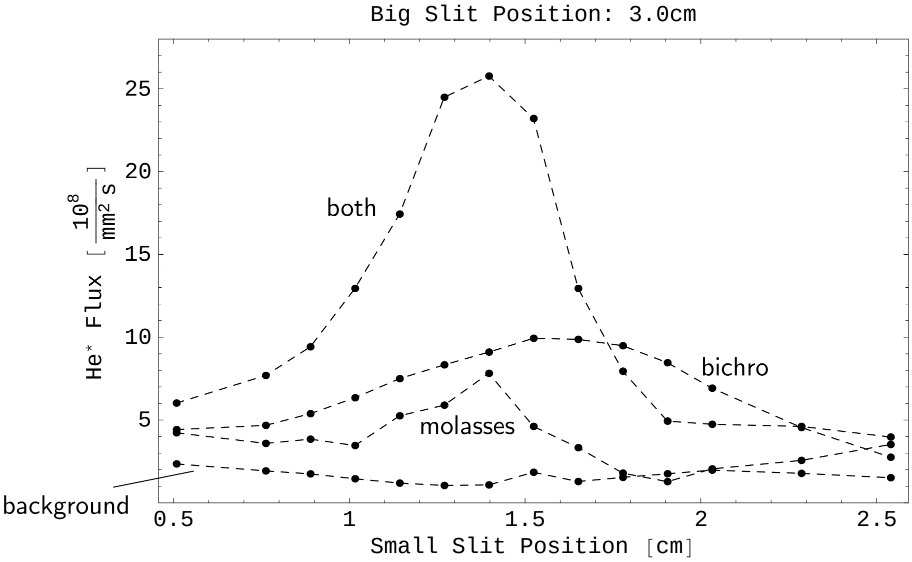

Figure A.4 Atomic beam cross section with the big slit of the SSD at 3.0 cm.

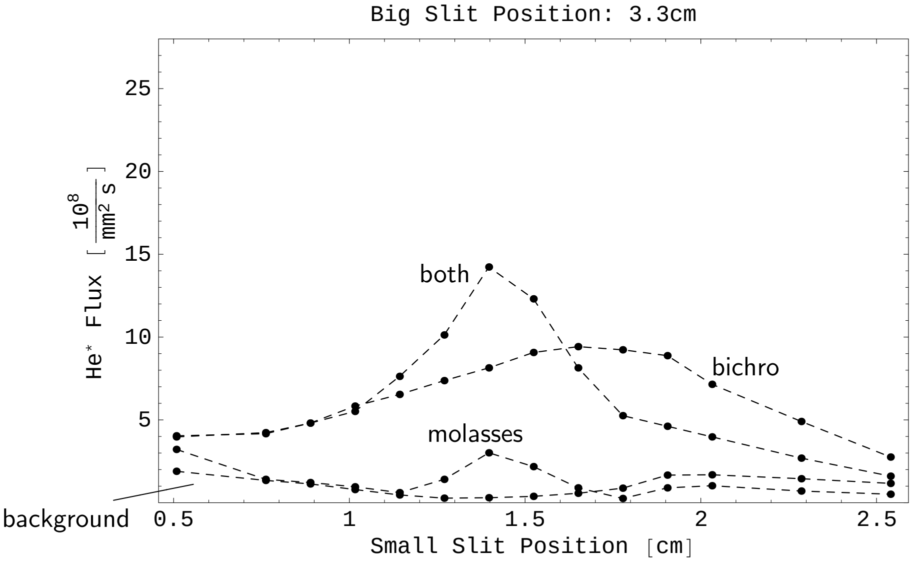

Figure A.5 Atomic beam cross section with the big slit of the SSD at 3.3 cm.